



HAL
open science

A 3-D Semianalytical Solution for Density-Driven Flow in Porous Media

Qian Shao, Marwan Fahs, Hussein Hoteit, Jesús Carrera, Philippe Ackerer,
Anis Younes

► **To cite this version:**

Qian Shao, Marwan Fahs, Hussein Hoteit, Jesús Carrera, Philippe Ackerer, et al.. A 3-D Semianalytical Solution for Density-Driven Flow in Porous Media. *Water Resources Research*, 2018, 54 (12), pp.10,094-10,116. 10.1029/2018WR023583 . hal-02105126

HAL Id: hal-02105126

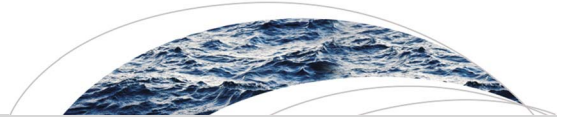
<https://hal.science/hal-02105126>

Submitted on 18 Nov 2021

HAL is a multi-disciplinary open access archive for the deposit and dissemination of scientific research documents, whether they are published or not. The documents may come from teaching and research institutions in France or abroad, or from public or private research centers.

L'archive ouverte pluridisciplinaire **HAL**, est destinée au dépôt et à la diffusion de documents scientifiques de niveau recherche, publiés ou non, émanant des établissements d'enseignement et de recherche français ou étrangers, des laboratoires publics ou privés.

Copyright



Water Resources Research

RESEARCH ARTICLE

10.1029/2018WR023583

Key Points:

- A 3-D semianalytical solution for the density-driven flow model is developed, for the first time, using Fourier series method
- The solution is used to gain physical insight into 3-D density-driven flow processes in the case of horizontal crossed density gradients
- Numerical simulations, using COMSOL and advanced research code, show the worthiness of the semianalytical solution for benchmarking 3-D codes

Correspondence to:

M. Fahs,
fahs@unistra.fr

Citation:

Shao, Q., Fahs, M., Hoteit, H., Carrera, J., Ackerer, P., & Younes, A. (2018). A 3-D semianalytical solution for density-driven flow in porous media. *Water Resources Research*, 54, 10,094–10,116. <https://doi.org/10.1029/2018WR023583>

Received 28 JUN 2018

Accepted 17 NOV 2018

Accepted article online 26 NOV 2018

Published online 17 DEC 2018

A 3-D Semianalytical Solution for Density-Driven Flow in Porous Media

Qian Shao¹, Marwan Fahs² , Hussein Hoteit³, Jesus Carrera⁴ , Philippe Ackerer², and Anis Younes^{2,5,6} 

¹School of Civil Engineering, Wuhan University, Wuhan, PR China, ²Laboratoire d'Hydrologie et Geochemie de Strasbourg, University of Strasbourg/EOST/ENGEEs, Strasbourg, France, ³Physical Science and Engineering Division, King Abdullah University of Science and Technology, Thuwal, Saudi Arabia, ⁴Institute of Environmental Assessment and Water Research (IDAEA), CSIC, Barcelona, Spain, ⁵IRD UMR LISAH, Montpellier, France, ⁶Laboratoire de Modélisation en Hydraulique et Environnement, Ecole Nationale d'Ingénieurs de Tunis, Tunis, Tunisia

Abstract Existing analytical and semianalytical solutions for density-driven flow (DDF) in porous media are limited to 2-D domains. In this work, we develop a semianalytical solution using the Fourier Galerkin method to describe DDF induced by salinity gradients in a 3-D porous enclosure. The solution is constructed by deriving the vector potential form of the governing equations and changing variables to obtain periodic boundary conditions. Solving the 3-D spectral system of equations can be computationally challenging. To alleviate computations, we develop an efficient approach, based on reducing the number of primary unknowns and simplifying the nonlinear terms, which allows us to simplify and solve the problem using only salt concentration as primary unknown. Test cases dealing with different Rayleigh numbers are solved to analyze the solution and gain physical insight into 3-D DDF processes. In fact, the solution displays a 3-D convective cell (actually a vortex) that resembles the quarter of a torus, which would not be possible in 2-D. Results also show that 3-D effects become more important at high Rayleigh number. We compare the semianalytical solution to research (Transport of RadioActive Elements in Subsurface) and industrial (COMSOL Multiphysics®) codes. We show cases (high Rayleigh number) where the numerical solution suffers from numerical artifacts, which highlight the worthiness of our semianalytical solution for code verification and benchmarking. In this context, we propose quantitative indicators based on several metrics characterizing the fluid flow and mass transfer processes and we provide open access to the source code of the semianalytical solution and to the corresponding numerical models.

1. Introduction

Density-driven flow (DDF) in saturated porous media may occur when the density of the fluid in place is perturbed from compositional or temperature changes (Diersch & Kolditz, 2002; Simmons, 2005; Simmons et al., 2010). Lateral density variations lead to the formation of natural convection cells (Abarca et al., 2007). In the case of both thermal and compositional variations, double diffusion-convection phenomena, also known as thermohaline convection, may take place (Nield & Bejan, 2017; Zhu et al., 2017). Numerical modeling of DDF is an essential tool for groundwater resources management and energy applications (Holzbecher, 1998) as DDF may occur in different phenomena such as, seawater intrusion in coastal aquifers (Werner et al., 2013), dense contaminant plume migration (Zhang & Schwartz, 1995), saltwater fingering under sabkha and saline lakes (Nield et al., 2008), saltwater upconing under freshwater lenses (Gingerich et al., 2017; Ketabchi et al., 2014), geothermal systems (Nguyen et al., 2016), hydrocarbon reservoir initialization (Hoteit & Firoozabadi, 2018; Riley & Firoozabadi, 1998), underground nuclear waste disposal, and geological carbon sequestration (see Niemi et al., 2017, and references therein).

It is well recognized that DDF processes occur in 3-D. However, a common practice is to perform simulations in 2-D to reduce the computational overhead (e.g., Graf & Boufadel, 2011; Hidalgo & Carrera, 2009; Xie et al., 2011). The validity of 2-D simulations relies on the assumption that the variations in rock, fluid properties, and boundary conditions (BCs) are negligible in the third dimension. With the advancement of computational power, 3-D DDF simulations have become more affordable and numerous academic and industrial software packages support 3-D DDF simulations, such as FEFLOW (Diersch, 2014), d3f (Schneider et al., 2012), HydroGeo-Sphere (Therrien et al., 2010), MODFLOW (Langevin et al., 2017),

SUTRA (Voss & Provost, 2010), SEAWAT (Langevin et al., 2008), OpenGeoSys (Sachse et al., 2015), and COMSOL Multiphysics.

Several studies demonstrated the necessity of 3-D DDF simulations as 2-D models may not be representative. For instance, Abarca et al. (2007) analyzed the effect of aquifer topography on seawater intrusion and emphasized that such effects can only be captured by 3-D DDF models. Doulgeris and Zissis (2014) concluded that 3-D models were needed to evaluate pumping schemes in coastal aquifers. Kerrou and Renard (2010) developed 2-D and 3-D models and highlighted the need for 3-D models to investigate the effects of heterogeneity on seawater intrusion. Wang et al. (2010) pointed out the influence of 3-D inclinations on thermal natural convection in a porous cavity under stable and unstable conditions. Several authors have discussed the representativeness of 2-D and 3-D simulations for fingering instabilities due to variations in temperature and/or salinity (Johannsen et al., 2006; Knorr et al., 2016; Pau et al., 2010; Wang et al., 2016).

Despite the efforts made on the development of 3-D DDF models (e.g.; Hirthe & Graf, 2012; Miller et al., 2013; Moortgat et al., 2016; Povich et al., 2013), several questions related to the reliability, accuracy, and robustness of such models are not fully understood (Miller et al., 2013). In this context, analytical solutions are relevant because they may help to understand and test the numerical accuracy and convergence of 3-D numerical models. Analytical solutions are also convenient to analyze and understand physical processes, as they are free of numerical artifacts. They can also be used for sensitivity analysis and for parameter estimation. Most importantly, analytical solutions can serve as a benchmarking tool to assess the consistency and accuracy of numerical simulators in general and specifically for DDF (Kolditz et al., 2016; Stoeckl et al., 2016; Voss et al., 2010). As argued by Voss et al. (2010), a crucial step in the benchmarking procedure is to check against analytical solutions as this step can answer the question of whether or not a simulator is able to correctly solve the governing equations.

Only few analytical solutions are available for DDF problems in spite of their relevance due to the complexity of the mathematical model, and those solutions are limited to 2-D geometries. The semianalytical solution for saltwater intrusion in coastal aquifers, known as the Henry (1964) problem, has been widely used for numerical codes verification, but is limited to a case where buoyancy effects are dominated by diffusion. Fahs et al. (2014) developed new semianalytical solutions for DDF in a 2-D porous cavity for which the requirement of diffusion dominance has been alleviated. To our knowledge, analytical solutions for DDF in 3-D are unavailable. The existing 3-D benchmarks consist of matching simulations with laboratory experiments (e.g., Oswald et al., 1997; Oswald & Kinzelbach, 2004) or cross-checking among various simulators. Voss et al. (2010) proposed a procedure to verify 3-D codes based on the critical transition Rayleigh number when modeling unstable natural convection in an inclined cubic porous box.

In this work, we develop a semianalytical solution for a DDF problem in 3-D based on the Fourier Galerkin (FG) method. We describe the solution procedure in detail and grant open access to the source code. Three test cases with different Rayleigh numbers are discussed to analyze the solution behavior and to demonstrate its consistency with numerical solutions obtained by a research simulator Transport of RadioACTIVE Elements in Subsurface (TRACES [Hoteit, Ackerer, Mosé, Erhel, et al., 2004, Hoteit, Ackerer, & Mosé, 2004]) and an industrial simulator (COMSOL). These test cases highlight the worthiness of our semianalytical solution for code verification and benchmarking. Prasad and Simmons (2005) argue that quantitative indicators of flow and mass transfer are more relevant for code benchmarking than direct comparison of state variables maps because of instability and the qualitative nature of visual comparisons. Therefore, we propose and evaluate metrics analytically to provide quantitative indicators relevant for code benchmarking. Taking advantage of the developed semianalytical solution, we provide a clear and consistent understanding of the 3-D DDF processes involved. In fact, contrary to 2-D DDF processes in porous enclosures, which are well understood, relatively less investigation is available for 3-D processes. The most extensively studied 3-D configuration is the vertical density gradient where two different concentrations (or temperatures) are imposed at the domain top and bottom surfaces (e.g., Guerrero-Martínez et al., 2017; Johannsen et al., 2006; Oswald & Kinzelbach, 2004; Pau et al., 2010; Voss et al., 2010). However, Fajraoui et al. (2017) and Nield and Bejan (2017) reported some important situations (geological storage of carbon dioxide and geothermal reservoirs) in which the density gradient can be horizontal. Yet DDF processes in the case of horizontal density gradient have only been investigated in 2-D with a one-component density gradient along the y axis (Fahs et al., 2014; Shao et al., 2016; Sivasankaran et al., 2008). Here we use the developed semianalytical

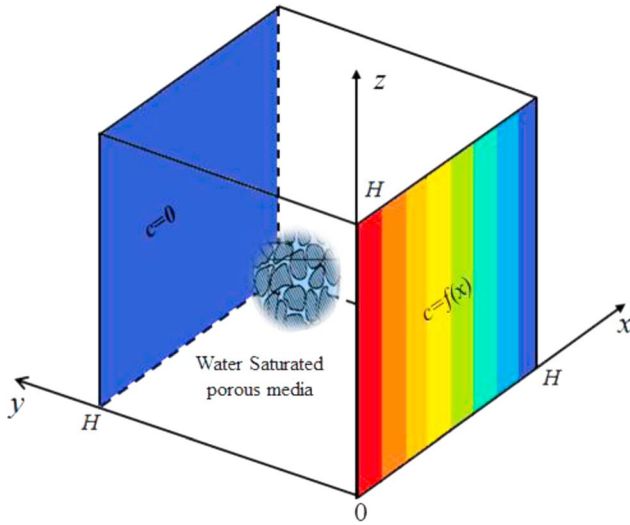


Figure 1. The conceptual problem of a cubic porous enclosure with varying boundary concentration on one side, constant concentration on the opposite side, and zero mass fluxes elsewhere.

solution to investigate the effect of 3-D crossed horizontal density gradient on flow and mass transport processes.

2. Problem and Model Statement

2.1. Problem Description

The problem under investigation is inspired by the benchmark model proposed by Voss et al. (2010). We consider a cubic porous enclosure of size H , as shown in Figure 1. The domain is saturated with water. All domain boundaries (six sides) are assumed impermeable so that fluid fluxes across the box sides are null. Salinity concentrations are imposed on two opposite sides creating salinity gradients across the domain. The imposed salinity concentration on the right vertical side of the domain (i.e., at $y = 0$) is a function of x ($c = f(x)$). On the opposite side of the domain (at $y = H$), the concentration is kept constant at 0 ($c = 0$). Thus, the salinity gradients are nonuniform, which result in a 3-D DDF problem induced by diffusion. Flow and transport occur under steady state conditions. The problem is set as a mass transport problem, but results can be recast to thermal effect if viscosity dependence with temperature is neglected. This 3-D problem is a generalization of the 2-D porous cavity problem studied by Fahs et al. (2014).

2.2. Model Assumptions

The mathematical model describing this DDF problem is based on the mass conservation equation, Darcy's law, and the salinity transport equation. We write these equations for transient conditions because later numerical approximations will be obtained as the steady state limit of transient simulations. We adopt the Boussinesq approximation (i.e., we neglect the product of density gradients times water flux). Similar to other existing 2-D semianalytical solutions, we take the dispersion tensor as isotropic and constant. Kalejaiye and Cardoso (2005) and Koohbor et al. (2018) showed that this assumption is valid when gravity is the main driving force and Rayleigh number is less than 1,000. Both conditions hold in our study. We assume density to vary linearly with concentration.

2.3. Governing Equations and BCs

Under these assumptions, the flow equation can be written in terms of the equivalent freshwater head as

$$S_s \frac{\partial h}{\partial t} + \nabla \cdot \mathbf{q} = 0, \quad (1)$$

$$\mathbf{q} = -\frac{\rho_0 g}{\mu} K \left(\nabla h + \frac{\rho(c) - \rho_0}{\rho_0} \mathbf{e}_z \right), \quad (2)$$

where $S_s [L^{-1}]$ is specific storage, $\rho [ML^{-3}]$ is fluid density, $h [L]$ is the equivalent freshwater head, $t [T]$ is time, $\mathbf{q} [LT^{-1}]$ is Darcy's velocity, $g [LT^{-2}]$ is gravity acceleration, $\mu [ML^{-1}T^{-1}]$ is the fluid dynamic viscosity, $K [L^2]$ is permeability, $\rho_0 [ML^{-3}]$ is the freshwater density, and \mathbf{e}_x , \mathbf{e}_y , and \mathbf{e}_z are the unit vectors of the Cartesian coordinate system.

Mass transport in the porous cavity is governed by the advection-dispersion equation:

$$\varepsilon \frac{\partial c}{\partial t} + \mathbf{q} \cdot \nabla c - \overline{D} \nabla \cdot \nabla c = 0, \quad (3)$$

where $c [-]$ is the relative solute concentration, ε is porosity, and $\overline{D} [L^2T^{-1}]$ is the dispersion coefficient.

In equation (2), the density is given by

$$\rho(c) = \rho_0 + (\rho_1 - \rho_0)c, \quad (4)$$

where ρ_1 is the saltwater density corresponding to $c = 1$.

At the steady state, equation (3) becomes

$$\mathbf{q}\nabla c - \varepsilon\overline{D}\nabla^2 c = 0. \quad (5)$$

The BCs are as follows:

$$\left\{ \begin{array}{l} q_x = 0 \\ \frac{\partial c}{\partial x} = 0 \end{array} \right. \text{ at } x = 0, H, \quad \left\{ \begin{array}{l} q_y = 0 \\ c = f(x) \\ q_y = 0 \\ c = 0 \end{array} \right. \text{ at } y = 0, H, \quad \text{and} \quad \left\{ \begin{array}{l} q_z = 0 \\ \frac{\partial c}{\partial z} = 0 \end{array} \right. \text{ at } z = 0, H, \quad (6)$$

where q_x , q_y , and q_z are the water flux (Darcy velocity) components in the x , y , and z directions, respectively.

3. Solution Methodology

Semianalytical solutions are often obtained in 2-D problems using the FG method (Peyret, 2013). Ameli et al. (2013) used the Fourier series method to solve saturated-unsaturated flow equations in multilayer unconfined aquifers. Fahs et al. (2014) developed a new implementation of the FG method and suggested a new 2-D benchmark for DDF. Shao et al. (2015, 2016) extended this implementation to natural convection in porous media in Darcy and Darcy-Brinkman regimes. Fahs et al. (2016) used the FG method to obtain the solution of the dispersive Henry problem. BniLam and Al-Khoury (2017), based on the spectral element method, developed an accurate solution for heat flow in shallow geothermal systems. The key idea of the FG method is to expand the unknowns into appropriate Fourier series that honor the BCs. The FG method requires periodic BCs, which are essential for the Fourier series expansion (Peyret, 2013). The streamline formulation of the governing equations has been used to obtain periodic flow BCs. The stream function formulation provides a robust and efficient solution that honors the continuity equation and allows eliminating the pressure variable from the momentum conservation equation.

In 3-D, however, the stream function is undefined. To overcome this challenge, we develop a different approach based on the vector potential, which is briefly outlined as follows:

1. The vector potential formulation of the governing equations is constructed by applying the curl operator to Darcy's law in 3-D. This approach leads to periodic flow BCs.
2. For the mass transport equation, an appropriate change of variable is applied to ensure periodic BCs (Fahs et al., 2014; van Reeuwijk et al., 2009).
3. The impermeable flow BCs result in a vanishing vertical component of the vector potential. The x and y components of the vector potential as well as the salt concentration are expanded in triple infinite Fourier series, which are truncated at a given order and appropriately substituted in the governing equations.
4. The equations are then multiplied by the Fourier modes and integrated over the 3-D domain. The triple integrals are evaluated analytically to derive the final system of nonlinear equations with the Fourier series coefficients as unknowns.
5. Convective terms of the transport equation lead to nonlinearity and involve six nested summations, which leads to a very CPU time demanding system of equations. Computational challenges are also related to convergence difficulties caused by the nonlinearity of the system.
6. To overcome these challenges, we develop a new approach based on reducing the degrees of freedom by expressing analytically the flow in terms of the salt concentration in the spectral space. Thus, the spectral equations are solved using the Fourier coefficients of the salt concentration as the primary unknowns. A sound implementation is developed, based on an advanced nonlinear solver and an appropriate algorithm, for the evaluation of the 3-D Fourier series and the nonlinear convective terms.

A detailed description of the solution method is discussed in the following sections.

4. The Fourier Series Solution

The solution approach is described in the four following steps.

4.1. The Vector Potential Formulation

At steady state, the velocity field (\mathbf{q}) admits a vector potential (ϕ), such that (Guerrero-Martínez et al., 2017; Hirasaki & Hellums, 1968; Luz Neto et al., 2006)

$$\mathbf{q} = \nabla \times \phi. \quad (7)$$

The vector potential in equation (7) satisfies the continuity equation, $\nabla \cdot \mathbf{q} = \nabla \cdot (\nabla \times \phi) = 0$. Applying the *curl* operator on Darcy's law allows the elimination of the freshwater head, as $\nabla \times \nabla h = 0$. Then, one can readily write

$$\nabla \times \nabla \times \phi = -\frac{gK(\rho_1 - \rho_0)}{\mu} \left(\frac{\partial c}{\partial y} \mathbf{e}_x - \frac{\partial c}{\partial x} \mathbf{e}_y \right). \quad (8)$$

The first term of equation (8) is expanded as

$$\nabla \times \nabla \times \phi = \nabla(\nabla \cdot \phi) - \nabla^2 \phi. \quad (9)$$

A solenoidal vector potential can be used as shown in Guerrero-Martínez et al. (2017) and Luz Neto et al. (2006), leading to $\nabla \cdot \phi = 0$. Therefore, in this case, equation (9) reduces to

$$\nabla \times \nabla \times \phi = -\nabla^2 \phi. \quad (10)$$

Significant expansion of this mathematical development is given in Appendix A.

Substitute equation (10) into equation (8), the flow equation becomes

$$\nabla^2 \phi - \frac{gK(\rho_1 - \rho_0)}{\mu} \left(\frac{\partial c}{\partial y} \mathbf{e}_x - \frac{\partial c}{\partial x} \mathbf{e}_y \right) = 0. \quad (11)$$

Using equations (7) and (5), the steady state transport equation simplifies to

$$(\nabla \times \phi) \cdot \nabla c - \varepsilon \bar{D} \nabla^2 c = 0. \quad (12)$$

Consider the following dimensionless variables:

$$\psi = \frac{\phi}{D\varepsilon}, X = \frac{x}{H}, Y = \frac{y}{H}, Z = \frac{z}{H}. \quad (13)$$

Using these variables, the dimensionless steady state flow and transport equations become

$$\nabla^2 \psi - Ra \left(\frac{\partial c}{\partial Y} \mathbf{e}_x - \frac{\partial c}{\partial X} \mathbf{e}_y \right) = 0, \quad (14)$$

$$(\nabla \times \psi) \cdot \nabla c - \nabla^2 c = 0, \quad (15)$$

where $Ra = \frac{gK(\rho_1 - \rho_0)H}{\mu \bar{D} \varepsilon}$ is the Rayleigh number, which expresses the ratio of buoyancy driven to diffusion-driven salt fluxes. This system of equations is similar to the one encountered in the problem of natural convection in cubic box (Guerrero-Martínez et al., 2017; Luz Neto et al., 2006).

4.2. BCs

To solve equations (14) and (15), it is necessary to express the flow BCs in terms of the vector potential. Let us consider the top surface boundary of the domain ($Z = 1$). Since this boundary is impervious, it can be regarded as an isosurface of the x and y components of the vector potential, that is, ψ_x and ψ_y are constant at $Z = 1$. With $\nabla \cdot \psi = \partial \psi_x / \partial X + \partial \psi_y / \partial Y + \partial \psi_z / \partial Z = 0$, one gets $\partial \psi_z / \partial Z = 0$. As shown in Luz Neto et al. (2006) and Guerrero-Martínez et al. (2017), the vector potential impervious BCs become

$$\begin{aligned}\frac{\partial \psi_x}{\partial X} = \psi_y = \psi_z = 0, & \quad \text{at } X = 0, 1, \\ \frac{\partial \psi_y}{\partial Y} = \psi_x = \psi_z = 0, & \quad \text{at } Y = 0, 1, \\ \frac{\partial \psi_z}{\partial Z} = \psi_x = \psi_y = 0, & \quad \text{at } Z = 0, 1.\end{aligned}\tag{16}$$

The flow BCs in equation (16) are periodic. For mass transport, periodic BCs are obtained from the following change of variable:

$$C = c + (Y - 1)f(X).\tag{17}$$

Using equation (17), the BCs in terms of the shifted concentration C become

$$\begin{aligned}\frac{\partial C}{\partial X} = (Y - 1)f'(X) & \quad \text{at } X = 0, 1, \\ C = 0 & \quad \text{at } Y = 0, 1, \\ \frac{\partial C}{\partial Z} = 0 & \quad \text{at } Z = 0, 1.\end{aligned}\tag{18}$$

The above BCs are periodic when the function $f(X)$ satisfies the condition, $f(0) = f(1) = 0$. In this work, we select a particular function that exhibits periodic BCs, such that

$$f(X) = \frac{1 + \cos(\pi X)}{2}.\tag{19}$$

The selected $f(X)$, with $f_{X=0} = 1$, and $f_{X=1} = 0$, allows evaluating all the Galerkin integrals analytically. Note that our solution method is not limited to this particular function, but applies to any other function that honors the periodic BCs, as discussed above.

The z -component of equation (14) implies $\nabla^2 \psi_z = 0$, which together with the BCs in equation (16), leads to $\psi_z = 0$. Therefore, the final system of equations becomes:

$$\nabla^2 \psi_x - Ra \frac{\partial C}{\partial Y} + Ra.f(X) = 0\tag{20}$$

$$\nabla^2 \psi_y + Ra \frac{\partial C}{\partial X} - Ra(Y - 1)f'(X) = 0\tag{21}$$

$$\begin{aligned}-\frac{\partial \psi_y}{\partial Z} \frac{\partial C}{\partial X} + \frac{\partial \psi_x}{\partial Z} \frac{\partial C}{\partial Y} + \left(\frac{\partial \psi_y}{\partial X} - \frac{\partial \psi_x}{\partial Y} \right) \frac{\partial C}{\partial Z} + \frac{\partial \psi_y}{\partial Z} (Y - 1)f'(X) \\ - f(X) \frac{\partial \psi_x}{\partial Z} - \left(\frac{\partial^2 C}{\partial X^2} + \frac{\partial^2 C}{\partial Y^2} + \frac{\partial^2 C}{\partial Z^2} \right) + (Y - 1)f''(X) = 0\end{aligned}\tag{22}$$

4.3. The Fourier Series Solution (FG Method)

The vector potential components ψ_x and ψ_y , and the shifted concentration C are expanded using infinite triple Fourier series, truncated at given orders, as follows:

$$\psi_x(X, Y, Z) = \sum_{i=0}^{N_i} \sum_{j=1}^{N_j} \sum_{k=1}^{N_k} A_{i,j,k} \cos(i\pi X) \sin(j\pi Y) \sin(k\pi Z)\tag{23}$$

$$\psi_y(X, Y, Z) = \sum_{l=1}^{N_l} \sum_{m=0}^{N_m} \sum_{n=1}^{N_n} B_{l,m,n} \sin(l\pi X) \cos(m\pi Y) \sin(n\pi Z),\tag{24}$$

$$C(X, Y, Z) = \sum_{u=0}^{N_u} \sum_{v=1}^{N_v} \sum_{w=0}^{N_w} E_{u,v,w} \cos(u\pi X) \sin(v\pi Y) \cos(w\pi Z),\tag{25}$$

where N_i , N_j , and N_k (respectively N_l , N_m , and N_n) are the truncation orders for the vector potential component ψ_x (respectively ψ_y) in the x , y , and z coordinates. N_u , N_v , and N_w are the truncation orders for the

concentration C . $A_{i,j,k}$, $B_{l,m,n}$ and $E_{u,v,w}$ are the Fourier series coefficients for the vector potential components ψ_x and ψ_y and the concentration C , respectively.

Equations (23)–(25) are then substituted into equations (20)–(22). The resulting equations are multiplied, respectively, by the trial functions:

$$\begin{aligned}\Lambda_{I,J,K}^{\psi_x} &= 8 \cos(I\pi X) \sin(J\pi Y) \sin(K\pi Z) \quad I = 0, \dots, Ni, J = 1, \dots, Nj, K = 1, \dots, Nk, \\ \Lambda_{L,M,N}^{\psi_y} &= 8 \sin(L\pi X) \cos(M\pi Y) \sin(N\pi Z) \quad L = 1, \dots, Nl, M = 0, \dots, Nm, N = 1, \dots, Nn, \\ \Lambda_{U,V,W}^C &= 8 \cos(U\pi X) \sin(V\pi Y) \cos(W\pi Z) \quad U = 0, \dots, Nu, V = 1, \dots, Nv, W = 0, \dots, Nw\end{aligned}$$

The above equations are then triple integrated over the cubic domain. This leads to the following system of nonlinear algebraic equations with coefficients $A_{i,j,k}$, $B_{l,m,n}$ and $E_{u,v,w}$ as unknowns:

$$\begin{aligned}RFx_{I,J,K} &= -\pi^2 (I^2 + \alpha_I J^2 + \alpha_I K^2) A_{I,J,K} - \frac{\alpha_I Ra}{\pi} \sum_{v=1}^{Nv} \sum_{w=0}^{Nw} v E'_{I,v,w} \Phi_{J,v} \Phi_{K,w} \\ &+ \frac{Ra}{\pi^2} \Phi_{J,0} \Phi_{K,0} \left(\delta_{I,0} + \frac{\delta_{I,1}}{2} \right) = 0 \\ &(I = 0, \dots, Ni, J = 1, \dots, Nj \text{ and } K = 1, \dots, Nk),\end{aligned}\tag{26}$$

$$\begin{aligned}RFy_{L,M,N} &= -\pi^2 (\alpha_M L^2 + M^2 + \alpha_M N^2) B_{L,M,N} - \frac{L Ra}{\pi} \sum_{v=1}^{Nv} \sum_{w=0}^{Nw} E'_{L,v,w} \Phi_{M,v} \Phi_{N,w} \\ &- Ra \cdot \delta_{L,1} \Phi_{N,0} \left(\frac{1 - (-1)^M}{\pi^2 (M - \delta_{M,0})} + \frac{\delta_{M,0}}{2} \right) = 0 \\ &(L = 1, \dots, Nl, M = 0, \dots, Nm \text{ and } N = 1, \dots, Nn),\end{aligned}\tag{27}$$

$$\begin{aligned}RT_{U,V,W} &= -\frac{\pi}{4} W \sum_{i=0}^{Ni} A'_{i,v,w} (2\alpha_U \delta_{U,i} + \delta_{U,1-i} + \delta_{U,i+1} + \delta_{U,i-1}) \\ &+ \frac{\pi}{4} W \sum_{l=1}^{Nl} \sum_{m=0}^{Nm} B'_{l,m,w} (\delta_{U,1-l} + \delta_{U,l-1} - \delta_{U,l+1}) \Gamma_{V,m} \\ &+ \pi^2 (\alpha_W U^2 + \alpha_W \alpha_U V^2 + \alpha_U W^2) E_{U,V,W} \\ &+ \frac{\pi^2}{8} \sum_{u=0}^{Nu} \sum_{v=1}^{Nv} \sum_{w=0}^{Nw} E_{u,v,w} \left[\sum_{i=0}^{Ni} \sum_{j=1}^{Nj} \sum_{k=1}^{Nk} A_{i,j,k} \zeta_{U,i,u} (k \cdot v \cdot \gamma_{V,j,v} \eta_{W,k,w} + j \cdot w \cdot \kappa_{V,j,v} \nu_{W,k,w}) \right. \\ &\left. + \sum_{l=1}^{Nl} \sum_{m=0}^{Nm} \sum_{n=1}^{Nn} B_{l,m,n} \kappa_{V,m,v} (n \cdot u \cdot \nu_{U,l,u} \eta_{W,n,w} - l \cdot w \cdot \eta_{U,l,u} \nu_{W,n,w}) \right] + \frac{2\pi}{V} \delta_{U,1} \delta_{W,0} = 0 \\ &(U = 0, \dots, Nu, V = 1, \dots, Nv \text{ and } W = 0, \dots, Nw),\end{aligned}\tag{28}$$

where RFx , RFy , and RT are the residuals corresponding to the flow and mass transport equations, respectively. The coefficients of equations (26)–(28) are given in Appendix B.

4.4. Implementation of the Fourier Series Solution

The rank of the nonlinear system obtained from equations (26) to (28) is $(Ni + 1) \times Nj \times Nk + Nl \times (Nm + 1) \times Nn + (Nu + 1) \times Nv \times (Nw + 1)$. To reduce the size of the system, we solve equations (26) and (27) for the coefficients $A_{i,j,k}$ and $B_{l,m,n}$ as a function of $E_{u,v,w}$. We then substitute $A_{i,j,k}$ and $B_{l,m,n}$ into equation (28), which needs to be solved for the coefficients $E_{u,v,w}$. Thus, in the spectral space, the governing equations can be solved with just the concentration as a primary unknown. We implemented an efficient solution of the spectral system in a FORTRAN code using the nonlinear solver of the IMSL library (<http://www.roguewave.com/products-services/imsl-numerical-libraries>). The solver is based on the modified Powell hybrid algorithm, which is an alternative to Newton's method. It has been successfully used with the FG method in Fahs et al. (2014, 2016). In this work, we evaluate the Jacobian matrix analytically as detailed in Appendix C.

Equation (28) involves six nested summations, and therefore, the computational complexity is of the order $O(Nu \times Nv \times Nw \times Ni \times Nj \times Nk + Nu \times Nv \times Nw \times Nl \times Nm \times Nn)$. The computations, although simple, are highly CPU consuming, which may defeat the purpose of having a fast exact solution. To address this challenge, we reformulate the system to reduce its computational complexity. In Appendix D, we show how the six nested

summations can be reduced to three and therefore reducing the complexity to $O(Nu \times Nv \times Nw)$. This simplification renders the Fourier series solution affordable as the computational time is reduced by 2 to 3 orders of magnitude. For instance, with about 6,500 Fourier modes, the computational time for the residual vector reduces from 61 to 0.13 s. The CPU gain becomes even more significant when the number of Fourier modes is increased. Further, we could reduce the computational time by another order of magnitude by using parallel computing on a multicore machine. The solution is already fast, however, we implement parallel computing to highlight that the FG method is highly parallelizable.

4.5. Evaluation of the Nondimensional Metrics

Mass transfer by diffusion into the domain (across the boundary side $Y = 0$) is assessed by the average Sherwood number (\overline{Sh}). This number is analogous to the Nusselt number in heat transfer problems. The local Sherwood number represents the ratio of the induced convective flux to the diffusive flux across the boundary ($Y = 0$), which is given by (Xie et al., 2012):

$$Sh = \frac{h_m}{\varepsilon \overline{D}/H}, \quad (29)$$

where h_m is the convection mass transfer coefficient.

The total mass flux can be calculated analogously to Newton's cooling law. The conservation of mass at the boundary $Y = 0$, between the induced convection and the diffusion fluxes, is written as

$$\frac{\varepsilon \overline{D}}{H} \frac{\partial c}{\partial Y} \Big|_{Y=0} = h_m c_{surf} \quad (30)$$

where c_{surf} is the imposed average concentration at the boundary $Y = 0$. In our case, we have

$$c_{surf} = \int_0^1 \int_0^1 f(X) dXdZ = 1/2$$

Therefore, the local Sherwood number can be expressed in terms of the concentration gradient:

$$Sh = \frac{1}{c_{surf}} \frac{\partial c}{\partial Y} \Big|_{Y=0} \quad (31)$$

Using the change of variable from equation (17) and the Fourier series expansion in equation (25), we obtain

$$Sh = \frac{\pi}{c_{surf}} \sum_{u=0}^{Nu} \sum_{v=1}^{Nv} \sum_{w=0}^{Nw} v E_{u,v,w} \cos(u\pi X) \cos(w\pi Z) - \frac{f(X)}{c_{surf}} \quad (32)$$

The average Sherwood number is defined by

$$\overline{Sh} = \int_0^1 \int_0^1 Sh.dXdZ = \frac{\pi}{c_{surf}} \sum_{v=1}^{Nv} v E_{0,v,0} - 1 \quad (33)$$

We now define the dimensionless velocity:

$$\mathbf{Q} = \frac{H}{D_e} \mathbf{q} \quad (34)$$

In the section 5 we discuss the significance of \mathbf{Q} and demonstrate how to use the maximum values of its components, Q_x^{\max} , Q_y^{\max} and Q_z^{\max} , to assess the flow behavior. These velocity components are calculated using the Fourier series expansions of ψ_x and ψ_y as well as the potential vector definition given in equation (7).

5. Results and Discussion

5.1. Test Cases and Solution Behavior

We analyze the behavior of the semianalytical solutions for three test cases with low (diffusion dominant), intermediate, and high (convection dominant) Rayleigh numbers that correspond to

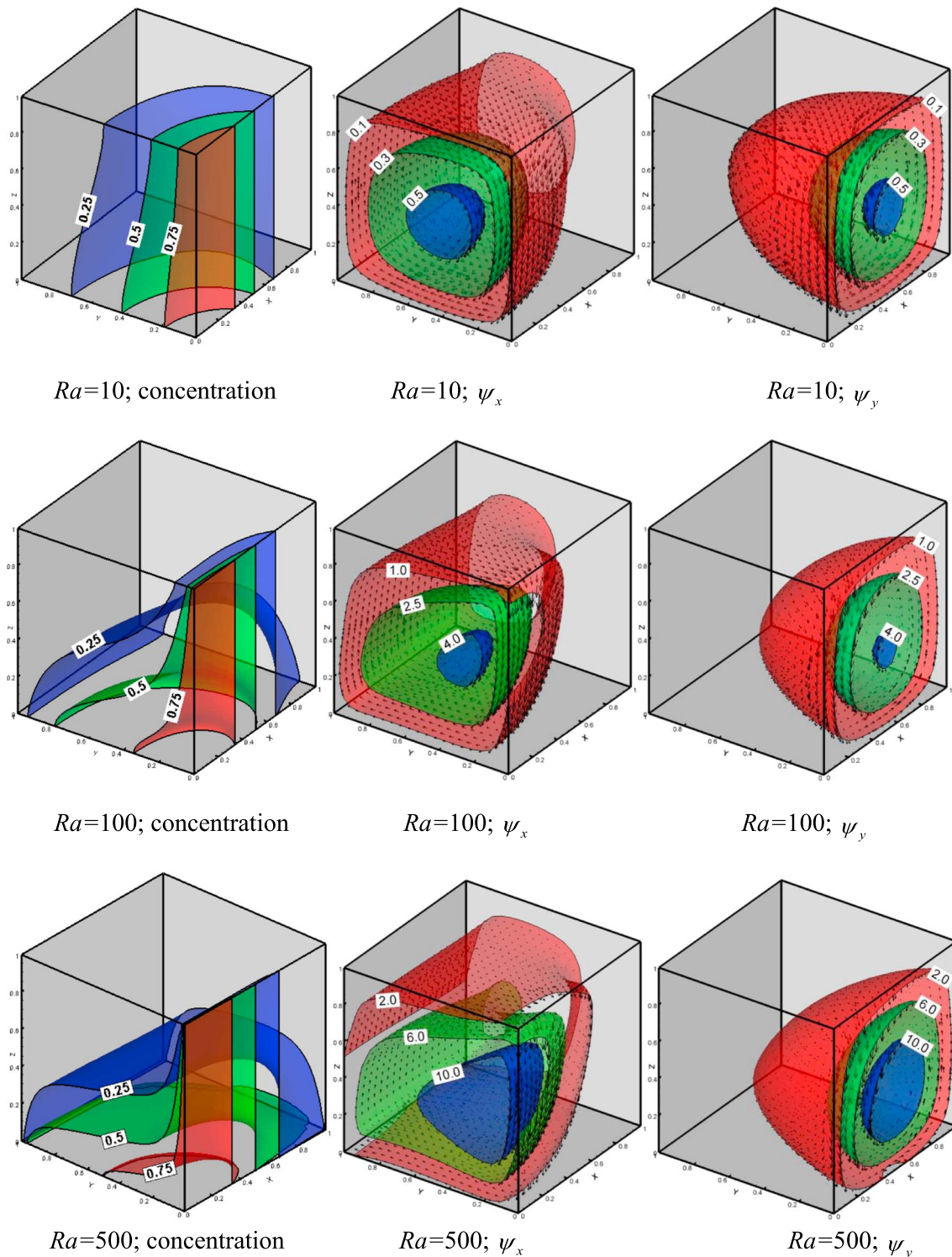


Figure 2. Isosurfaces of salt concentration (first column), x -component ψ_x (middle column) and y -component ψ_y (last column) of the vector potential for $Ra = 10, 100,$ and 500 . The velocity field (arrows) show the flow direction.

$Ra = 10, 100,$ and $500,$ respectively. Note that when Ra is below a critical value, mass transfer occurs primarily by diffusion, so that concentration contours are vertical. When Ra exceeds the critical value, buoyancy becomes relevant and mass transfer takes place also by convection, which causes concentration contours to become more intruded toward the bottom than the top of the

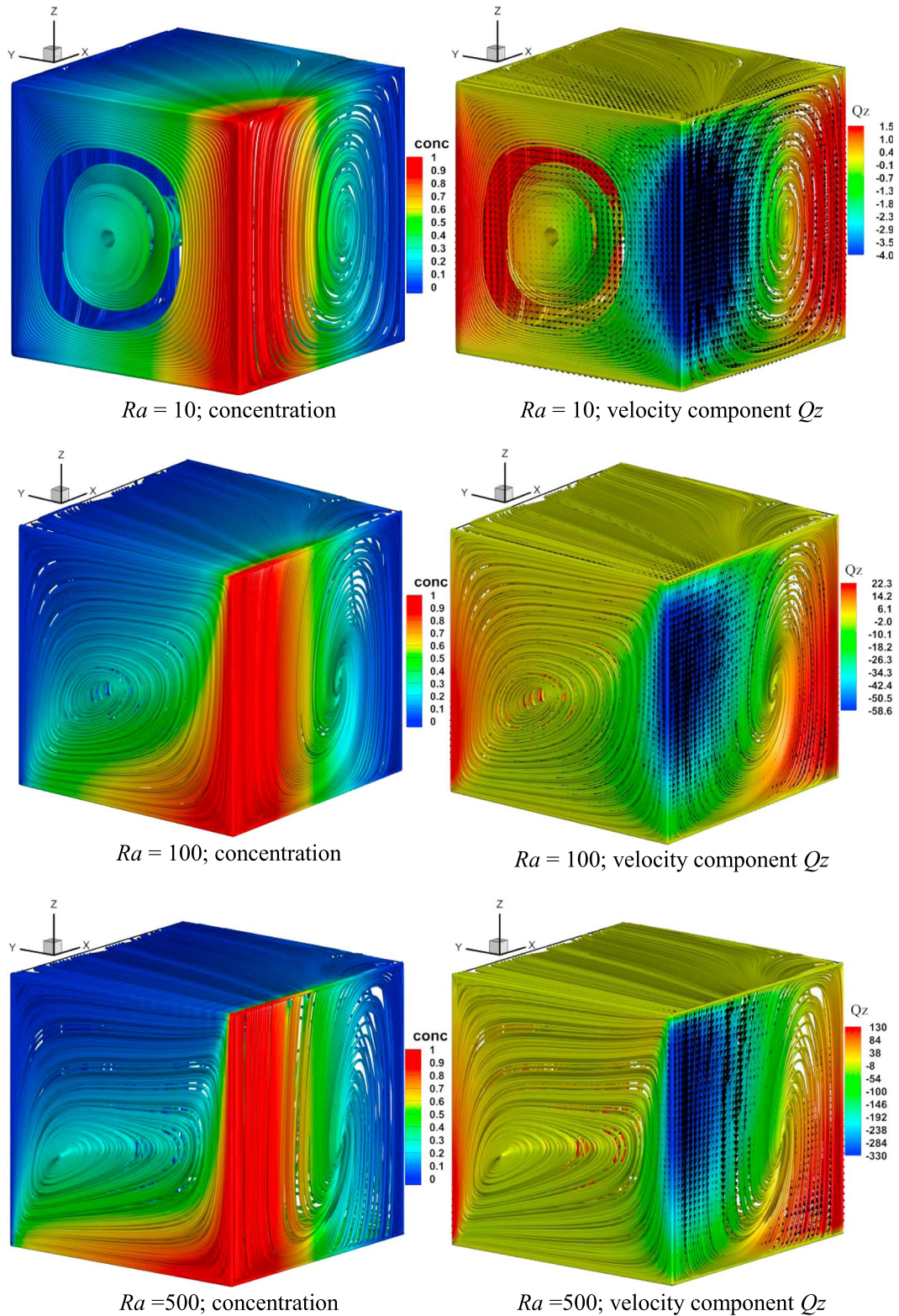


Figure 3. Stream tubes highlighted with concentration intensity (left); and with the vertical velocity component, Q_z , (right) for $Ra = 10, 100,$ and 500 . The velocity field (arrows) are superimposed on the plots to show the convection cells with flow direction.

Table 1
Fourier Series Solutions for the Three Test Cases: Number of Fourier Modes, Maximum Velocity Components and Average Sherwood Number

Ra	Nt	Q_x^{\max}	Q_y^{\max}	Q_z^{\max}	\overline{Sh}
10	648	2.56	2.55	5.41	1.04
100	4,536	25.07	31.22	62.22	2.47
500	8,424	86.98	131.64	337.89	6.96

domain. The three values of Ra considered in this work exceed the critical value for the onset of convection. The numerical convergence of the semianalytical solutions in terms of the Fourier modes is discussed in Appendix E.

The isosurfaces of the concentration (c) and the potential components (ψ_x and ψ_y), as well as the velocity fields are plotted in Figure 2. These isosurfaces show that the saltwater tends to intrude toward the bottom of the domain due to its higher density, as expected. As the Rayleigh number increases, the concentration distribution becomes steeper and the transition zone becomes narrower close to the top right corner (i.e., $X = 0$, $Y = 0$, and $Z = 1$). The isosurfaces of ψ_x and ψ_y confirm a three-dimensional flow behavior. They show that the bulk of the enclosure is occupied by a single 3-D rotating vortex. This is best illustrated by Figure 3, which shows the stream tubes highlighted with concentration intensity (left) and with the vertical component of Darcy's velocity (right), for $Ra = 10$, 100, and 500. The stream tubes illustrate the 3-D nature of the steady state convective cells.

An exciting feature of our solution is that the convection cell becomes a vortex with a torus-like shape with the Z axis at the origin as the axis of rotation. The convective cell (O-ring cell), as seen in the YZ plane at $X = 0$, looks like the conventional cells that would result in 2-D as a result of the imposed salinity gradient along the Y axis where $C_{Y=0} = 1$ and $C_{Y=1} = 0$ (i.e., to transfer mass from $Y = 0$ to $Y = 1$ across the cavity). The convective cell, as seen in the XZ face at $Y = 0$, is trickier. On the one hand, it results from the imposed salinity gradient along the X axis where $C_{X=0} = 1$ and $C_{X=1} = 0$ (i.e., to transfer mass from $X = 0$ to $X = 1$ within the $Y = 0$ face). On the other hand, since solute mass is entering the cavity throughout the face, it creates a concentration gradient and density contrasts in the Y direction, so as to favor mass transfer from the $Y = 0$ face to the $Y = 1$ face. The results are 3-D stream tubes spiraling around a quarter of a torus-like-shaped eddy formed by the revolution of the O-ring cell from the XZ to the YZ face around the Z axis. Unlike a torus, the O-rings are interconnected which can be seen at the center of the cells. That is, the stream tubes describe a vortex that starts at XZ face to die at the YZ face. The rotation direction (arrows) and the vertical velocity, Q_z , (color map) are shown on Figure 3 (right) for $Ra = 10$, 100, and 500, where increasing Ra intensifies the velocity field and modifies the concentration distribution and the shape of the convective cell. The center of the convective cell in the XZ plane (at $Y = 0$) moves away from the salted wall when Ra is increased. In the YZ plane at $X = 0$, the center of the rotating cell moves toward the bottom corner ($X = 0$, $Y = 1$, and $Z = 0$) when the Rayleigh number is increased. Figure 3 shows also that the concentration distribution follows more closely the flow stream tubes as the Rayleigh number increases, which indicates a convection-dominant flow regime.

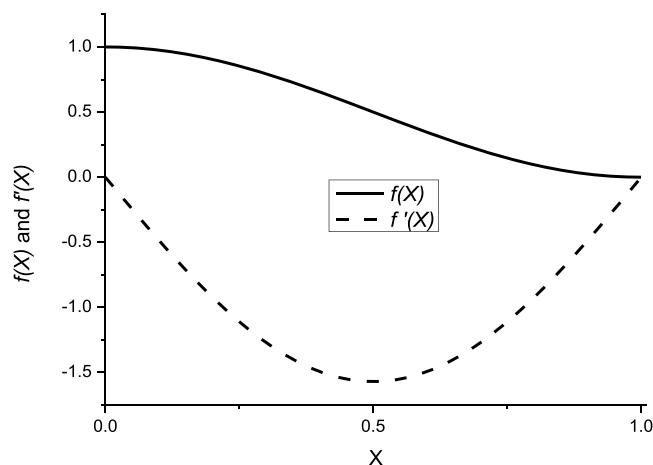


Figure 4. Variation of the boundary imposed concentration function $f(X)$ and its derivative $f'(X)$.

Table 1 summarizes the obtained average Sherwood number and maximum velocity components for the three test cases. This table indicates that, for $Ra = 10$, \overline{Sh} approaches the pure diffusive regime ($\overline{Sh} \rightarrow 1$). As expected, \overline{Sh} increases with Ra because the buoyancy-induced flow enhances the mass transfer across the domain boundary by increasing the concentration gradient and, thus, diffusive fluxes at the $Y = 0$ face (see left columns of Figures 2 and 3). As expected also, Table 1 indicates that the increase of Ra intensifies the rotating water flow within the porous box. It should be noted that the metrics presented in Table 1 represent a high-quality data suitable for convergence studies and for benchmarking. While the existing benchmarks are mainly based on subjective visual inspections, these metrics provide quantitative indicators that can be practical and rigorous for the evaluation of 3-D DDF models. For the three Ra cases, Q_x exhibits its largest value around the middle slice ($X = 0.5$), which corresponds to the maximum local density gradient $f'(X)$, as shown in Figure 4. The Q_x contour maps showing the intensity of Q_x with the streamlines for the three cases in the XZ plane (at $Y = 0$) are plotted in Figure 5.

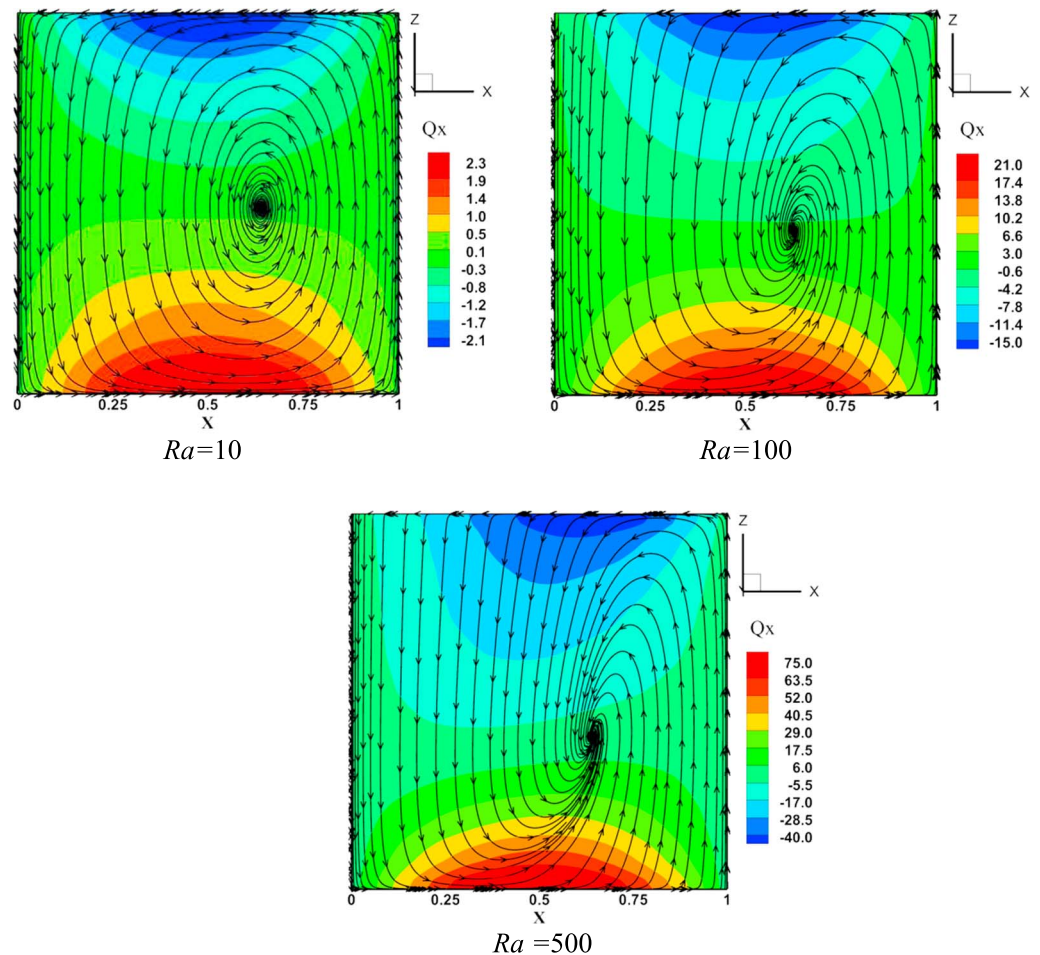


Figure 5. Velocity component (Q_x) contour maps and streamlines in the XZ plane (at $Y = 0$) demonstrating the maximum intensity near $X = 0.5$, where the vortex originates.

5.2. Verification and Worthiness of the 3-D Semianalytical Solution

We compare here our 3-D semianalytical solutions with two simulators for the three test cases discussed above ($Ra = 10, 100,$ and 500). The first simulator is TRACES (Hoteit, Ackerer, Mosé, Erhel, et al., 2004; Hoteit, Ackerer, & Mosé, 2004; Younes et al., 2009). This is an in-house research simulator for flow and reactive transport in saturated porous media that provides highly accurate numerical solutions by solving the transient flow and transport equations using appropriate numerical methods. The flow equations (1) and (2) are solved using the mixed hybrid finite element method with a fully implicit scheme for time integration (Abushaikha et al., 2017; Younes et al., 2010). The mixed hybrid finite element method provides accurate velocity field even in highly heterogeneous porous media. A time-splitting approach is used for the transport equation (3). The convection term of the transport equation is solved using the discontinuous Galerkin finite element method with an explicit time scheme. This method provides highly accurate solutions for hyperbolic systems (Miller et al., 2013). The dispersion term is discretized using the mixed hybrid finite element method with an implicit time scheme.

A computer code is developed to solve the nonlinear spectral system resulting from the FG method. This code should be checked to verify its correctness. Experiments that account for all the processes and BCs of the problem under investigation do not exist in the literature. Therefore, contrary to the standard practice (use analytical solutions to test numerical codes), the high accuracy of TRACES code allows us to test the correct implementation of our semianalytical solution. We used a cubic regular mesh to avoid inaccuracies and instabilities that can be introduced by the change in mesh sizes with irregular grids. The simulation domain is

Table 2
Physical Parameters Used in the Numerical Models (TRACES and COMSOL) for the Three Test Cases

Porous box side	$H = 1.0 \text{ m}$
Specific storage	$S_s = 10^{-11} \text{ m}^{-1}$ (in TRACES) and 0 (in COMSOL)
Permeability	$K = 1.022 \times 10^{-9} \text{ m}^2$
Porosity	$\varepsilon = 0.5$
Freshwater density	$\rho_0 = 998 \text{ kg/m}^3$
Saltwater density	$\rho_1 = 1,018 \text{ kg/m}^3$
Gravity	$g = 9.81 \text{ m/s}^2$
Viscosity	$\mu = 10^{-3} \text{ kg}\cdot\text{m}^{-1}\cdot\text{s}^{-1}$
Dispersion coefficient (m^2/s)	$\bar{D} = 4.006 \times 10^{-5}$ for $Ra = 10$ $\bar{D} = 4.006 \times 10^{-6}$ for $Ra = 100$ $\bar{D} = 8.012 \times 10^{-7}$ for $Ra = 500$

Note. TRACES = Transport of RadioActive Elements in Subsurface.

discretized into a uniform $60 \times 60 \times 60$ grid. This grid refinement with 216,000 (216K) cubic cells was found to achieve solution convergence with no grid dependence. The solution approach consists of letting the system evolve under transient conditions until steady state. The physical parameters used in the numerical code for the three cases are given in Table 2.

The values of the average Sherwood number and maximum velocity components obtained with TRACES are summarized in Table 3. TRACES and semianalytical concentration contours on a vertical cross section of the domain at $X = 0.5$ are plotted in Figure 6 (left). For quantitative comparison, we also calculated the average relative errors for concentration and velocity components, over all the domain (i.e., average of the errors calculated at the nodes of the computational mesh). The relative error for the concentration is defined as follows:

$$Er^C = \frac{1}{Nn} \frac{1}{C^{\max}} \sum_{i=1}^{Nn} |C_i^{An} - C_i^{Num}| \quad (35)$$

where Nn is the number of nodes in the computational mesh, C^{\max} is the maximum concentration in the domain, C_i^{An} is the semianalytical concentration on a node (i) and C_i^{Num} is the numerical concentration obtained using TRACES. The errors on the velocity components are defined in the same manner as in equation (35).

The average relative errors are given in Table 3. The largest value is observed for the concentration at $Ra = 500$, but it is less than 1%. Table 3 (compared to Table 2) and Figure 6 show excellent agreement between the semianalytical and TRACES solutions for all cases. These results give more confidence to the semianalytical code and highlights the robustness of TRACES.

The second simulator is COMSOL Multiphysics®. This test is meant to evaluate the worthiness of the developed semianalytical solution for codes benchmarking because one of the main contributions of this paper is to provide 3-D semianalytical solutions that can be used as a reference for benchmarking 3-D DDF codes. Benchmarking is needed to verify that the results of codes are free of numerical artifacts, which may affect the accuracy of the predicted results, parameter estimation procedures, and sensitivity analysis outcomes (Esfandiari et al., 2015; Nassar & Ginn, 2014). A common requirement for a useful benchmark problem is that it allows examination of the performance of numerical techniques implemented in the codes. Thus, this section focuses on the evaluation of the ability of the proposed semianalytical solutions for benchmarking numerical methods and techniques that are commonly used in DDF codes. COMSOL offers a variety of numerical techniques that can be used to solve the governing equations. The COMSOL model was built using the same physical parameters as in TRACES (Table 2). We first use COMSOL with the standard finite element method and implicit time-stepping scheme with adaptive time step size based on the second-order

Table 3
Numerical Solutions (TRACES and COMSOL) for the Three Test Cases ($Ra = 10, 100$, and 500): Maximum Velocity Components, Average Sherwood Number and Relative Errors

Ra	Q_x^{\max}	Q_y^{\max}	Q_z^{\max}	\bar{Sh}	Er^{Q_x} (%)	Er^{Q_y} (%)	Er^{Q_z} (%)	Er^C (%)
TRACES								
10	2.79	2.74	5.37	1.04	0.14	0.21	0.27	0.30
100	24.39	29.72	60.86	2.47	0.22	0.29	0.35	0.31
500	87.91	124.44	336.77	6.97	0.34	0.54	0.44	0.98
COMSOL								
10	2.96	2.80	5.72	1.04	0.90	0.92	0.93	0.02
100	26.26	38.89	68.45	2.48	0.26	0.36	0.32	0.47
500	109.49	158.73	425.30	6.95	1.45	3.16	1.78	5.40

Note. TRACES = Transport of RadioActive Elements in Subsurface.

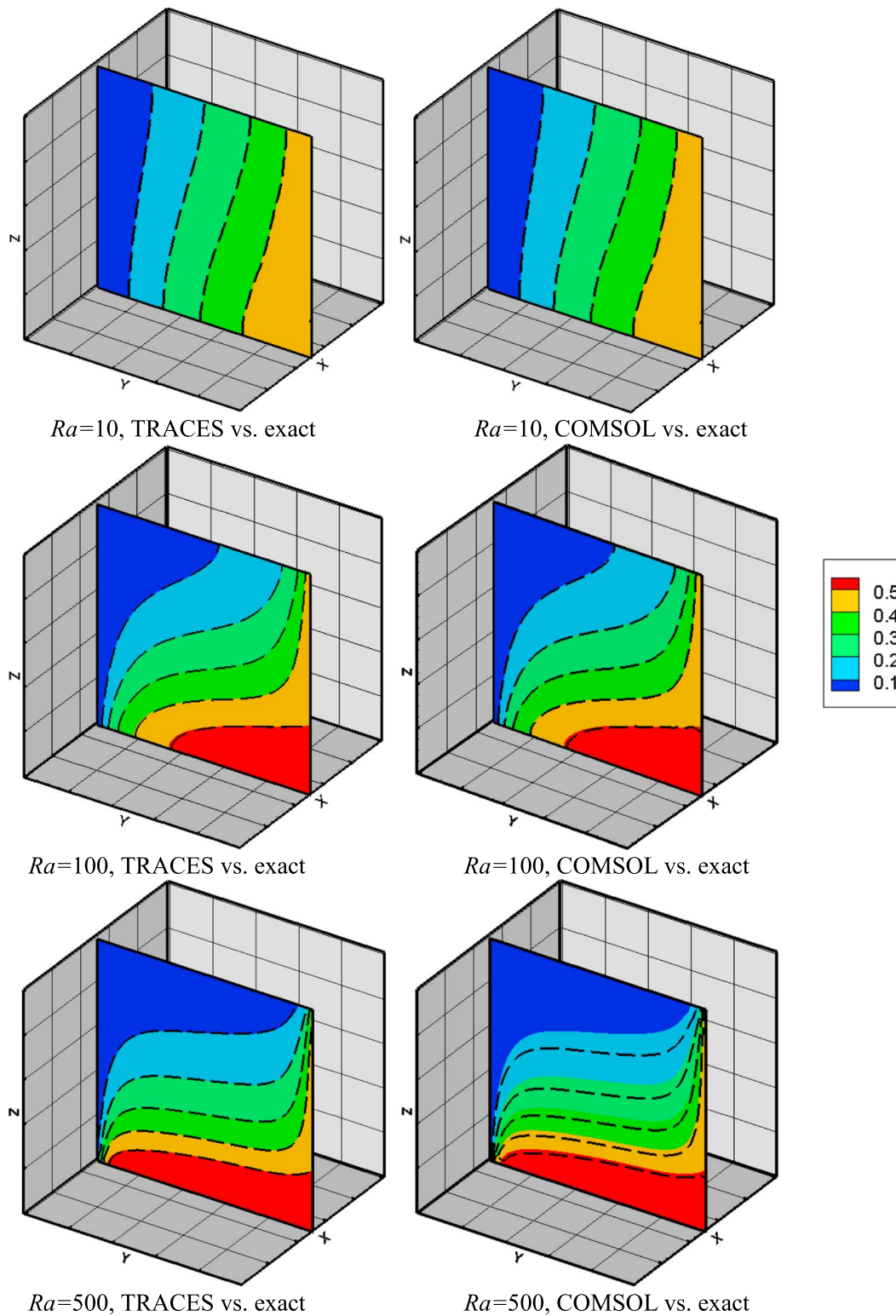


Figure 6. Concentration contours at the vertical slice $X = 0.5$. Comparison of the semianalytical solutions (colored map), referred to as *exact*, and numerical solutions (dashed lines) for the three cases; comparison with TRACES is on the left and comparison with COMSOL is on the right. TRACES = Transport of RadioActive Elements in Subsurface.

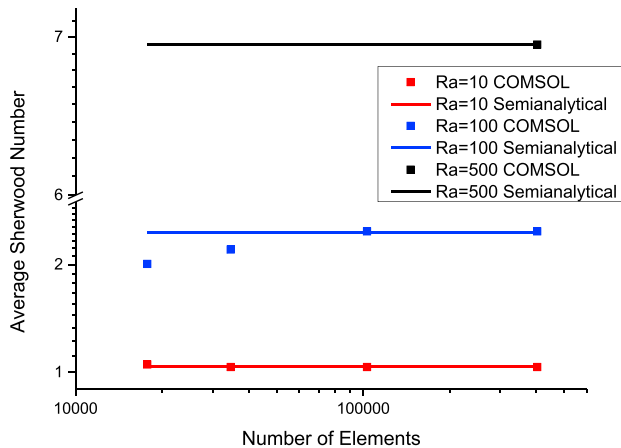


Figure 7. Grid sensitivity analysis for the solutions with standard finite element method in COMSOL (the method failed to converge for coarse grids when $Ra = 500$).

backward differentiation formula. Transient simulations are performed. The duration of the simulation is selected to be 9 hr to reach steady state.

A grid sensitivity analysis was performed to assess numerical convergence. The refinement levels consist of about 17K, 34K, 103K, and 402K elements (tetrahedral), respectively. The average Sherwood number involves the spatial derivative of the concentration. We find it to be a reliable metric to assess the gridding effect. Fahs et al. (2014) provided a detailed analysis of the sensitivity of the Sherwood number to the grid and noted that when this number becomes independent of the mesh size all the solution patterns (concentration and velocity field) become stable. Here we propose to use \bar{Sh} as an indicator to assess the gridding effect for the COMSOL solutions. As shown in Figure 7, the COMSOL solution for $Ra = 10$ is the same for all mesh refinements. Grid effects become more pronounced with $Ra = 100$. The average Sherwood numbers, \bar{Sh} , and maximum velocity components obtained with COMSOL are summarized in Table 3. As for TRACES, the relative errors for concentration and velocity components are less than 1% (Table 3). Both cases with $Ra = 10$ and 100 show excellent agreement with the semianalytical solution as depicted in Figure 6 (right) and Table 3.

For $Ra = 500$, COMSOL experienced convergence problems. No convergence to the steady state could be obtained with the coarse grids due to unphysical oscillations that appeared in the concentration solutions. Examples of these oscillations are plotted in Figure 8. It is observed that the oscillations mainly appear around the high gradient concentration zones and spread in the whole domain. These oscillations lead to incoherent results with, for instance, negative concentrations and concentration values larger than 1. They cause the convergence of the linearization procedure to stall or to fail as the discrete system of equations becomes ill conditioned. These oscillations can be removed by using very fine grids, which can be computationally excessive in 3-D. With the finest grid size that we tested, which consisted of about 400K elements, the COMSOL model could converge to the steady state solution. With the fine model, oscillations could be significantly reduced but the grid refinement was still not fine enough to match the semianalytical solution and concentrations are in the range (-0.24) to (1.34) . The corresponding concentration contours (Figure 6), average Sherwood number and maximum velocity components (Table 3) show less agreement between the semianalytical and COMSOL solutions than the other cases (i.e., $Ra = 10$ and 100), especially for the low concentration contour and the maximum velocity components (Table 3).

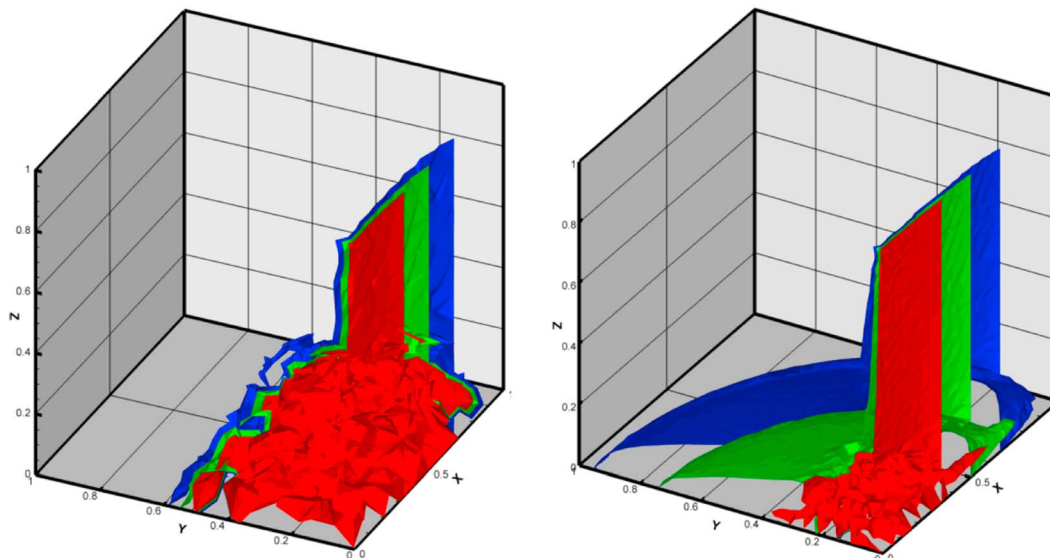


Figure 8. Spurious oscillations in the COMSOL solutions for $Ra = 500$ with coarse grids, solution stability improves with finer grid (right).

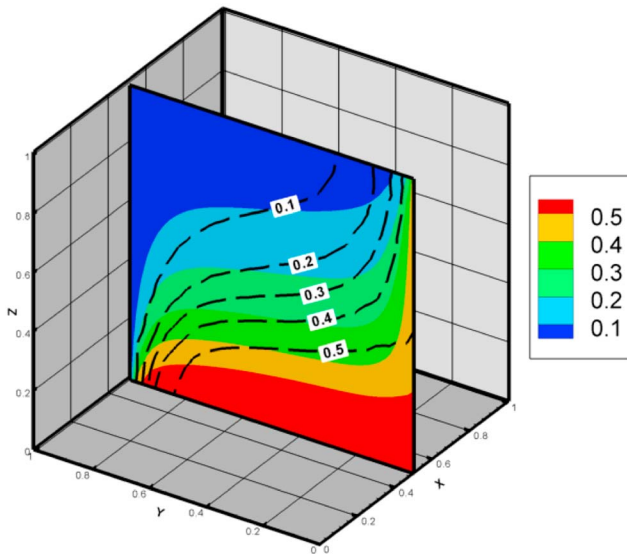


Figure 9. Comparison between the semianalytical solution (color map) and COMSOL with the stabilization technique (dashed line) for $Ra = 500$. COMSOL results are obtained using the grid size with 103K elements. Discrepancy between both solutions is related to the excessive numerical diffusion introduced by the stabilization technique in COMSOL.

We also tried using the stabilization techniques implemented in COMSOL, which are based on adding artificial diffusion. They improved convergence but the solution diverted further from the semianalytical solution because of excessive numerical diffusion (Figure 9). It should be noted that with the in-house model, we did not encounter any issue related to the unphysical oscillations or numerical diffusion. This is due to the use of higher-order Discontinuous Galerkin and mixed finite element methods. We also performed additional COMSOL runs using a variable-order backward differentiation formula scheme, but no significant improvement was observed. No further refinements were attempted in COMSOL because of impractical computational run time, which is in the range of several days.

5.3. Three-Dimensional DDF Processes in the Case of Horizontal Crossed Density Gradients

The developed semianalytical solution describes DDF in 3-D with crossed horizontal density gradients (two coplanar components along the x and y axes). Thus, we take advantage of this semianalytical solution to provide a better understanding of the 3-D DDF processes in such a case. We particularly aim to investigate the effect of the normal component of the density gradient (x component) on mass transfer and convective flow. To do so, we replaced the boundary concentration (equation (19)) by $f(X) = \frac{1+\omega \cos(\pi X)}{2}$ with ω a parameter between 0 and 1. This function gives the same average (0.5) for all values of ω . The increase of ω leads to the

increase of the x component of the density gradient (XCDG). For $\omega = 0$, $XCDG = 0$; thus, the problem can be simplified to 2-D. The effect of ω on the average Sherwood number is given in Figure 10a. This figure shows that the increase in ω leads to the increase of \overline{Sh} . Figure 10b depicts the effect of ω on the convective flow. For the sake of brevity, we only present the variation of Q_x^{\max} . Similar behavior has been observed for Q_y^{\max} and Q_z^{\max} . Figure 10b shows that the increase of ω intensifies the rotating convective flow. As it can be seen in Figure 10, the effect of ω on the mass transfer to the domain and on the convective flow is more significant for high Rayleigh numbers.

The effect of ω on the concentration distribution is investigated at the slice $X = 0.5$, at which the XCDG exhibits its maximum value (see Figure 4). This slice is relevant as it reflects the proper effect of the XCDG on the mass transfer to the domain. In fact, in this slice, the y component of the density gradient is constant (independent of ω) as the imposed concentrations are 0.5 and 0 at the right and left sides, respectively. Thus, the change in ω affects only the XCDG. The effect of ω on the concentration distribution is given in Figure 11. For $Ra = 10$, the salinity distribution is slightly sensitive to ω . The concentration ranges between 0 and 0.5, which

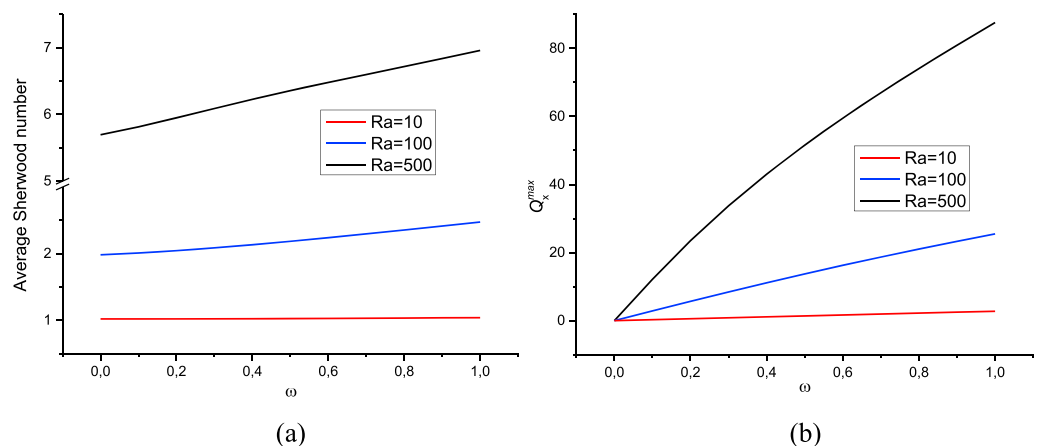


Figure 10. Effect of ω (the parameter controlling the x component of the density gradient) on \overline{Sh} and Q_x^{\max} .

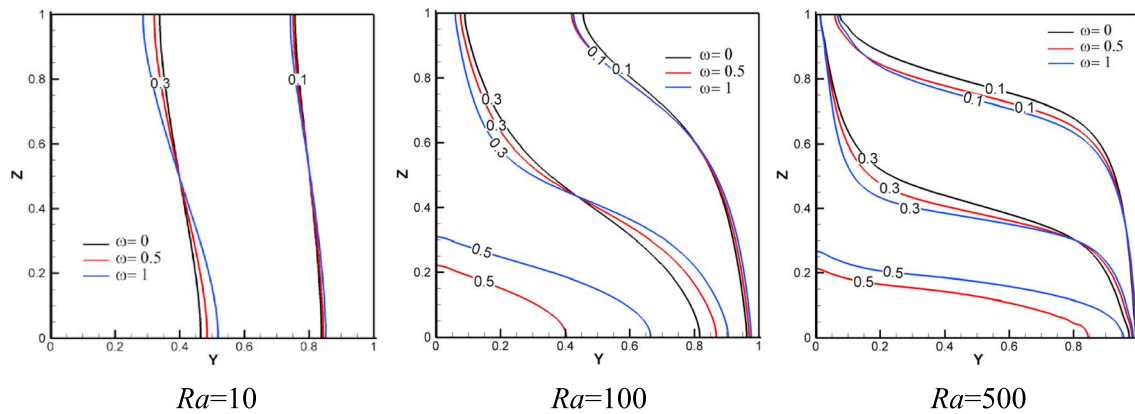


Figure 11. Effect of ω on the concentration distribution in the slice $X = 0.5$.

indicates that there is no mass transfer by convection along the x axis, as this process should increase the salinity above 0.5. The concentration contours are very similar to those corresponding to the 2-D case ($\omega = 0$). This confirms that the effect of the XCDG is insignificant at low Rayleigh regimes. For $Ra = 100$, ω mainly affects the high concentration contours (0.3 and 0.5) in the region closed to the salted side. The influence of ω spatially expands and reaches the low salinity contours at higher Rayleigh number ($Ra = 500$). For high Rayleigh numbers ($Ra = 100$ and 500), buoyancy effects, which are related to the XCDG, overcome the diffusion processes and lead to the apparition of a convective flow in parallel to the plane (XOZ). Toward the box bottom surface, the convective flow, generated by the XCDG, yields the apparition of the high-salinity pocket at the right bottom corner of the porous box (at $X = 0$, $Y = 0$, and $Z = 0$). The salt concentration in this zone exceeds the concentration imposed on the right wall. This result indicates that the XCDG effects become more pronounced at high Rayleigh regimes.

6. Summary and Conclusions

Existing semianalytical solution of DDF model are limited to 2-D cases. In this work we developed the first 3-D semianalytical solution. The solution describes DDF processes generated by two horizontal crossed salinity gradients (one in the x direction and one in the y direction) in a porous box. The solution was derived by applying the Fourier series method to the vector potential form of the governing equations. The vector potential form simplifies the system of equations by eliminating the pressure and satisfying the continuity equation. A specific change of variable has been applied to the concentration, which leads to periodic BCs. The components of the vector potential and the concentration were then expanded into infinite Fourier series that satisfied the BCs. A Galerkin treatment was then applied using the Fourier modes as trial functions. In the spectral space, the flow was expressed analytically in terms of the concentration. This leads to a final spectral nonlinear system with the Fourier series coefficients of the concentration as primary unknowns. A new approach was then developed to simplify the six nested Fourier series to only three, which helped to reduce the computational time by 2 to 3 orders of magnitude. From the technical point of view, an important feature for this work is the generalization of the FG method to 3-D problems. Indeed, the FG method is typically restricted to 2-D solutions. This work shows that, with an efficient implementation, the FG method can be extended to 3-D.

We have analyzed our semianalytical solution for three test cases with $Ra = 10$, 100 , and 500 . A unique feature of the solution is the development of a vortex as a mass transfer mechanism. The vortex displays a quarter of a torus-like shape. A benchmark with two simulators was then provided. The solutions showed good agreements with an in-house code based on advanced finite element methods. Good agreement with COMSOL has been obtained except for the case with high Ra number. Grid sensitivity analysis was then discussed. For $Ra = 500$, COMSOL solution showed spurious oscillations on coarse grids, which prevented convergence. Very fine mesh (more than 500K elements) was needed to improve agreement with the semianalytical solution. Accurate simulation of this particular case is a real challenge for standard 3-D DDF simulators because of impractical computational time.

The developed semianalytical solution provided an unambiguous benchmark for verifying, testing and comparing numerical simulators. Fourier series have been used to derive metrics to characterize the flow and

mass transport processes using the Sherwood number and the maximum velocity components. These metrics are practical and rigorous quantitative indicators that can be used to evaluate DDF models.

Three-dimensional DDF processes are not well understood yet and have not been investigated in the literature for the case of crossed horizontal density gradients. Thus, we used the semianalytical solution to provide physical insight on the DDF processes in such a case. The results showed that the normal density gradient increases the mass transfer to the domain and intensifies the rotating convective flow. The effect of the normal density gradient became more important for high Rayleigh regime. For practical usage in further studies, we provide open access to the source code of our semianalytical solution on the author's website (<https://lhyges.unistra.fr/FAHS-Marwan>) and the corresponding COMSOL models on the COMSOL application exchange website.

Appendix A: Potential Vector Formulation of the Flow Equation

The vector potential can be defined component-wise as

$$\begin{aligned} q_x &= \frac{\partial \varphi_z}{\partial y} - \frac{\partial \varphi_y}{\partial z}, \\ q_y &= \frac{\partial \varphi_x}{\partial z} - \frac{\partial \varphi_z}{\partial x}, \\ q_z &= \frac{\partial \varphi_y}{\partial x} - \frac{\partial \varphi_x}{\partial y}. \end{aligned} \quad (A1)$$

It is easy to verify that the potential vector satisfies the continuity equation $\nabla \cdot \mathbf{q} = \nabla \cdot (\nabla \times \boldsymbol{\varphi}) = 0$. By applying the *curl* operator on Darcy's law (equation (2)), we obtain

$$\nabla \times \mathbf{q} = -\frac{\rho_0 g}{\mu} K \left(\nabla \times \nabla h + \nabla \times \left(\frac{\rho - \rho_0}{\rho_0} \mathbf{e}_z \right) \right). \quad (A2)$$

We have $\nabla \times \nabla h = 0$ and $\rho - \rho_0 = (\rho_1 - \rho_0)c$. By developing $\nabla \times \left(\frac{\rho - \rho_0}{\rho_0} \mathbf{e}_z \right)$, we get

$$\nabla \times \mathbf{q} = -\frac{gK(\rho_1 - \rho_0)}{\mu} \left(\frac{\partial c}{\partial y} \mathbf{e}_x - \frac{\partial c}{\partial x} \mathbf{e}_y \right). \quad (A3)$$

In the other side we have

$$\nabla \times \mathbf{q} = \nabla \times \nabla \times \boldsymbol{\varphi} = \begin{bmatrix} \frac{\partial}{\partial x} \left(\frac{\partial \varphi_x}{\partial x} + \frac{\partial \varphi_y}{\partial y} + \frac{\partial \varphi_z}{\partial z} \right) - \frac{\partial^2 \varphi_x}{\partial x^2} - \frac{\partial^2 \varphi_x}{\partial y^2} - \frac{\partial^2 \varphi_x}{\partial z^2} \\ \frac{\partial}{\partial y} \left(\frac{\partial \varphi_x}{\partial x} + \frac{\partial \varphi_y}{\partial y} + \frac{\partial \varphi_z}{\partial z} \right) - \frac{\partial^2 \varphi_y}{\partial x^2} - \frac{\partial^2 \varphi_y}{\partial y^2} - \frac{\partial^2 \varphi_y}{\partial z^2} \\ \frac{\partial}{\partial z} \left(\frac{\partial \varphi_x}{\partial x} + \frac{\partial \varphi_y}{\partial y} + \frac{\partial \varphi_z}{\partial z} \right) - \frac{\partial^2 \varphi_z}{\partial x^2} - \frac{\partial^2 \varphi_z}{\partial y^2} - \frac{\partial^2 \varphi_z}{\partial z^2} \end{bmatrix} = \nabla(\nabla \cdot \boldsymbol{\varphi}) - \nabla^2 \boldsymbol{\varphi}. \quad (A4)$$

If we select a solenoidal vector potential ($\nabla \cdot \boldsymbol{\varphi} = 0$), equation (A4) leads to equation (11).

Appendix B: Coefficients and Matrices of the Nonlinear System (Equations (26)–(28))

The coefficient of spectral system (equations (26)–(28)) are given as follows:

$$\zeta_{G,r,s} = \delta_{G,r-s} + \delta_{G,r+s} + \delta_{G,s-r} + \delta_{G,-s-r}, \quad (B1)$$

$$\gamma_{G,r,s} = \delta_{G,r+s} - \delta_{G,s-r} + \delta_{G,r-s} \quad v_{G,r,s} = \delta_{G,r-s} - \delta_{G,r+s} + \delta_{G,s-r}, \quad (B2)$$

$$\kappa_{G,r,s} = \delta_{G,r+s} + \delta_{G,s-r} - \delta_{G,r-s} \quad v_{G,r,s} = \delta_{G,r-s} - \delta_{G,r+s} + \delta_{G,s-r}, \quad (B3)$$

$$\alpha_G = \begin{cases} 2 & \text{if } G = 0, \\ 1 & \text{if } G \neq 0, \end{cases} \quad (B4)$$

where $\delta_{i,j}$ is the Kronecker delta function.

$$\Phi_{G,r} = \begin{cases} \frac{1 - (-1)^{G+r}}{G+r} + \frac{1 - (-1)^{G-r}}{G-r} & \text{if } r \neq G \\ 0 & \text{if } r = G \end{cases} \quad (B5)$$

$$\Gamma_{G,r} = \begin{cases} \frac{1}{G+r} + \frac{1}{G-r} & \text{if } r \neq G \\ 0 & \text{if } r = G \end{cases} \quad (B6)$$

$$A'_{i,v,w} = \begin{cases} A_{i,v,w} & \text{if } V \leq N_j \text{ and } W \leq N_k \\ 0 & \text{else} \end{cases} \quad (B7)$$

$$B'_{l,m,w} = \begin{cases} B_{l,m,w} & \text{if } W \leq N_n \\ 0 & \text{else} \end{cases} \quad (B8)$$

$$E'_{G,v,w} = \begin{cases} E_{G,v,w} & \text{if } G \leq N_u \\ 0 & \text{else} \end{cases} \quad (B9)$$

Appendix C: The Jacobian Matrix

The Jacobian matrix requires the derivatives of the residual equations (RFx , RFy , and RT) with respect to the unknowns (the Fourier modes $A_{i,j,k}$, $B_{l,m,n}$ and $E_{u,v,w}$). These derivatives are calculated as follows:

$$\frac{\partial RFx_{I,J,K}}{\partial A_{i,j,k}} = -\pi^2 (I^2 + \alpha_j J^2 + \alpha_l K^2) \delta_{I,i} \delta_{J,j} \delta_{K,k} \quad (C1)$$

$$\frac{\partial RFx_{I,J,K}}{\partial E_{u,v,w}} = -\frac{\alpha_l Ra.v}{\pi} \Phi_{J,v} \Phi_{K,w} \delta_{I,u} \quad (C2)$$

$$\frac{\partial RFy_{L,M,N}}{\partial B_{l,m,n}} = -\pi^2 (\alpha_M L^2 + M^2 + \alpha_m N^2) \delta_{L,l} \delta_{M,m} \delta_{N,n} \quad (C3)$$

$$\frac{\partial RFy_{L,M,N}}{\partial E_{u,v,w}} = -\frac{L.Ra}{\pi} \Phi_{M,v} \Phi_{N,w} \delta_{L,u} \quad (C4)$$

$$\begin{aligned} \frac{\partial RT_{U,V,W}}{\partial A_{i,j,k}} &= -\frac{\pi}{4} W \delta_{V,j} \delta_{W,k} (2\alpha_U \delta_{U,i} + \delta_{U,1-i} + \delta_{U,i+1} + \delta_{U,i-1}) \\ &+ \frac{\pi^2}{8} \sum_{u=0}^{Nu} \sum_{v=1}^{Nv} \sum_{w=0}^{Nw} E_{u,v,w} \zeta_{U,i,u} (k.v.\gamma_{V,j,v} \eta_{W,k,w} + j.w.\kappa_{V,j,v} \nu_{W,k,w}) \end{aligned} \quad (C5)$$

$$\begin{aligned} \frac{\partial RT_{U,V,W}}{\partial B_{l,m,n}} &= \frac{\pi}{4} W \delta_{W,n} (\delta_{U,1-l} + \delta_{U,l-1} - \delta_{U,l+1}) \Gamma_{V,m} \\ &+ \frac{\pi^2}{8} \sum_{u=0}^{Nu} \sum_{v=1}^{Nv} \sum_{w=0}^{Nw} E_{u,v,w} \kappa_{V,m,v} (n.u.\nu_{U,l,u} \eta_{W,n,w} - l.w.\eta_{U,l,u} \nu_{W,n,w}) \end{aligned} \quad (C6)$$

$$\begin{aligned} \frac{\partial RT_{U,V,W}}{\partial E_{u,v,w}} &= \pi^2 (\alpha_W U^2 + \alpha_V \alpha_U V^2 + \alpha_U W^2) \delta_{U,u} \delta_{V,v} \delta_{W,w} \\ &+ \frac{\pi^2}{8} \left[\sum_{j=0}^{Nj} \sum_{k=1}^{Nk} A_{i,j,k} \zeta_{U,i,u} (k.v.\gamma_{V,j,v} \eta_{W,k,w} + j.w.\kappa_{V,j,v} \nu_{W,k,w}) \right. \\ &\left. + \sum_{l=1}^{Nl} \sum_{m=0}^{Nm} \sum_{n=1}^{Nn} B_{l,m,n} \kappa_{V,m,v} (n.u.\nu_{U,l,u} \eta_{W,n,w} - l.w.\eta_{U,l,u} \nu_{W,n,w}) \right] \end{aligned} \quad (C7)$$

Appendix D: Simplification of the Convective Term

Let us consider the terms involving six overlapped summations in equation (28). And we split them into four subterms, which read

$$Term1_{U,V,W} = \frac{\pi^2}{8} \sum_{u=0}^{Nu} \sum_{v=1}^{Nv} \sum_{w=0}^{Nw} \sum_{i=0}^{Ni} \sum_{j=1}^{Nj} \sum_{k=1}^{Nk} k.v.E_{u,v,w} A_{i,j,k} \zeta_{U,i,u} \gamma_{V,j,v} \eta_{W,k,w} \quad (D1)$$

$$Term2_{U,V,W} = \frac{\pi^2}{8} \sum_{u=0}^{Nu} \sum_{v=1}^{Nv} \sum_{w=0}^{Nw} \sum_{i=0}^{Ni} \sum_{j=1}^{Nj} \sum_{k=1}^{Nk} j.w.E_{u,v,w} A_{i,j,k} \zeta_{U,i,u} \kappa_{V,j,v} \nu_{W,k,w} \quad (D2)$$

$$Term3_{U,V,W} = \frac{\pi^2}{8} \sum_{u=0}^{Nu} \sum_{v=1}^{Nv} \sum_{w=0}^{Nw} \sum_{l=1}^{Nl} \sum_{m=0}^{Nm} \sum_{n=1}^{Nn} n.u.E_{u,v,w} B_{l,m,n} \nu_{U,l,u} \kappa_{V,m,v} \eta_{W,n,w} \quad (D3)$$

$$Term4_{U,V,W} = -\frac{\pi^2}{8} \sum_{u=0}^{Nu} \sum_{v=1}^{Nv} \sum_{w=0}^{Nw} \sum_{l=1}^{Nl} \sum_{m=0}^{Nm} \sum_{n=1}^{Nn} l.w.E_{u,v,w} B_{l,m,n} \eta_{U,l,u} \kappa_{V,m,v} \nu_{W,n,w} \quad (D4)$$

Now we take equation (D1), for example, reducing the six overlapped summations to only three. Substituting the coefficients in Appendix B into equation (D1), we obtain

$$Term1_{U,V,W} = \frac{\pi^2}{8} \sum_{u=0}^{Nu} \sum_{v=1}^{Nv} \sum_{w=0}^{Nw} \sum_{i=0}^{Ni} \sum_{j=1}^{Nj} \sum_{k=1}^{Nk} k.v.E_{u,v,w} A_{i,j,k} (\delta_{U,j-u} + \delta_{U,i+u} + \delta_{U,u-i} + \delta_{U,-u-i}) (\delta_{V,j+v} - \delta_{V,v-j} + \delta_{V,j-v}) (\delta_{W,k-w} + \delta_{W,k+w} + \delta_{W,w-k}) \quad (D5)$$

Expanding equation (D5) leads to 36 subterms as follows:

$$Term1_{U,V,W} = \frac{\pi^2}{8} \sum_{u=0}^{Nu} \sum_{v=1}^{Nv} \sum_{w=0}^{Nw} \sum_{i=0}^{Ni} \sum_{j=1}^{Nj} \sum_{k=1}^{Nk} k.v.E_{u,v,w} A_{i,j,k} \delta_{U,j-u} \delta_{V,j+v} \delta_{W,k-w} + \frac{\pi^2}{8} \sum_{u=0}^{Nu} \sum_{v=1}^{Nv} \sum_{w=0}^{Nw} \sum_{i=0}^{Ni} \sum_{j=1}^{Nj} \sum_{k=1}^{Nk} k.v.E_{u,v,w} A_{i,j,k} \delta_{U,j-u} \delta_{V,j+v} \delta_{W,k+w} + \dots + \frac{\pi^2}{8} \sum_{u=0}^{Nu} \sum_{v=1}^{Nv} \sum_{w=0}^{Nw} \sum_{i=0}^{Ni} \sum_{j=1}^{Nj} \sum_{k=1}^{Nk} k.v.E_{u,v,w} A_{i,j,k} \delta_{U,-u-i} \delta_{V,j-v} \delta_{W,w-k} \quad (D6)$$

Considering the properties of Kronecker delta function, we obtain the following relations:

$$\delta_{U,j-u} = \delta_{i,U+u}; \delta_{V,j+v} = \delta_{j,V-v}; \delta_{W,k-w} = \delta_{k,W+w}; \quad (D7)$$

$$\sum_u \sum_v \sum_w \sum_i \sum_j \sum_k E_{u,v,w} A_{i,j,k} \delta_{i,U+u} \delta_{j,V-v} \delta_{k,W+w} = \sum_u \sum_v \sum_w E_{u,v,w} A_{u,v,w} \quad (D8)$$

Using equations (D7) and (D8), the first term in equation (D6) can be simplified to

$$\frac{\pi^2}{8} \sum_{u=0}^{Nu} \sum_{v=1}^{Nv} \sum_{w=0}^{Nw} \sum_{i=0}^{Ni} \sum_{j=1}^{Nj} \sum_{k=1}^{Nk} k.v.E_{u,v,w} A_{i,j,k} \delta_{U,j-u} \delta_{V,j+v} \delta_{W,k-w} = \frac{\pi^2}{8} \sum_{u=0}^{Nu} \sum_{v=1}^{Nv} \sum_{w=0}^{Nw} (W + w).v.E_{u,v,w} A_{u+u,v-v,w+w} \quad (D9)$$

Table E1
Truncation Levels Used for Computation of Fourier Galerkin Solution

Level	N_x	N_y	N_z
1	3	3	3
2	3	9	3
3	3	12	6
4	3	15	9
5	3	18	15
6	3	24	21
7	3	30	24
8	3	39	24
9	3	39	30

Applying the same procedure to all terms in equation (D6), one can simplify the evaluation of the nonlinear convective term to three nested summations.

Appendix E: Convergence of Fourier Series Solution

Appropriate Fourier modes should be used to avoid Gibbs phenomenon and obtain oscillation-free solutions (Ameli et al., 2013; Peyret, 2013). Here we assess the stability of the semianalytical solution in terms of the

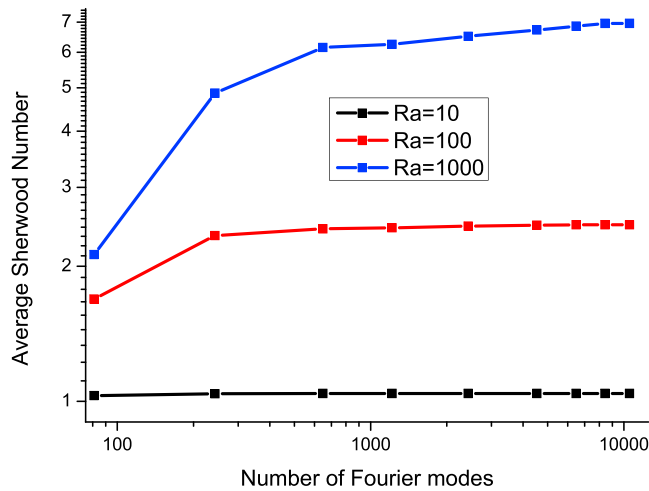


Figure E1. Variation of the average Sherwood number (\overline{Sh}) versus the total number of Fourier modes.

Fourier modes. To do so, we investigate the solution stability by increasing the number of Fourier modes. First runs of the semianalytical code showed that \overline{Sh} is the most sensitive metric to the number of Fourier modes. This makes sense as \overline{Sh} involves the first derivative of the salt concentration Fourier series and as the concentration distribution is sharper than the vector potential components. Thus, we consider the semianalytical solution to be stable when \overline{Sh} becomes independent of the number of Fourier modes, as \overline{Sh} is the most sensitive variable to the Fourier modes. In fact, \overline{Sh} involves the first derivatives.

For the sake of simplicity, same truncation orders are used for the Fourier series expansions of ψ_x , ψ_y , and C . Thus, we consider $N_x = N_i + 1 = N_l = N_u + 1$, $N_y = N_j = N_m + 1 = N_v$, and $N_z = N_k = N_n = N_w + 1$. We tested nine levels of truncation orders, as shown in Table E1. For the three considered test cases ($Ra = 10, 100$, and 500), the variations of the average Sherwood number versus the number of Fourier modes are given in Figure E1, which demonstrates the convergence of Fourier series solutions. The semianalytical solution for $Ra = 10$ has been obtained using 648 Fourier modes ($N_x = 3, N_y = 12$, and

$N_z = 6$). For higher Rayleigh numbers, the problem becomes convection dominant, and therefore, the solution is less smooth, which results in higher number of Fourier modes for convergence. For $Ra = 100$ and 500 we used 4,536 ($N_x = 3, N_y = 24$, and $N_z = 21$) and 8,424 ($N_x = 3, N_y = 39$, and $N_z = 24$) Fourier modes, respectively.

Acknowledgments

Q. Shao acknowledges the support of the National Natural Science Foundation of China (Grant 11702199) and the Natural Science Foundation of Hubei Province (Grant 2017CFB147). The Editor, Associate Editor, and the three reviewers are thanked for their comments that helped us to improve the paper. The source code for the semianalytical solution (with all necessary input files) as well as the TRACES model are available at <https://lhyges.unistra.fr/FAHS-Marwan> or by contacting the author directly (fahs@unistra.fr). The COMSOL models are available on the COMSOL application exchange website.

References

- Abarca, E., Carrera, J., Sánchez-Vila, X., & Voss, C. I. (2007). Quasi-horizontal circulation cells in 3D seawater intrusion. *Journal of Hydrology*, 339(3–4), 118–129. <https://doi.org/10.1016/j.jhydrol.2007.02.017>
- Abushaikha, A. S., Voskov, D. V., & Tchelepi, H. A. (2017). Fully implicit mixed-hybrid finite-element discretization for general purpose subsurface reservoir simulation. *Journal of Computational Physics*, 346, 514–538. <https://doi.org/10.1016/j.jcp.2017.06.034>
- Ameli, A. A., Craig, J. R., & Wong, S. (2013). Series solutions for saturated–unsaturated flow in multi-layer unconfined aquifers. *Advances in Water Resources*, 60, 24–33. <https://doi.org/10.1016/j.advwatres.2013.07.004>
- BniLam, N., & Al-Khoury, R. (2017). A spectral element model for nonhomogeneous heat flow in shallow geothermal systems. *International Journal of Heat and Mass Transfer*, 104, 703–717. <https://doi.org/10.1016/j.ijheatmasstransfer.2016.08.055>
- Diersch, H.-J. G., & Kolditz, O. (2002). Variable-density flow and transport in porous media: Approaches and challenges. *Advances in Water Resources*, 25(8–12), 899–944. [https://doi.org/10.1016/S0309-1708\(02\)00063-5](https://doi.org/10.1016/S0309-1708(02)00063-5)
- Diersch, H.-J. G. (2014). *FEFLOW*. Berlin: Springer. <https://doi.org/10.1007/978-3-642-38739-5>
- Doulgeris, C., & Zissis, T. (2014). 3D variable density flow simulation to evaluate pumping schemes in coastal aquifers. *Water Resources Management*, 28(14), 4943–4956. <https://doi.org/10.1007/s11269-014-0766-0>
- Esfandiari, B., Porta, G., Perotto, S., & Guadagnini, A. (2015). Impact of space-time mesh adaptation on solute transport modeling in porous media. *Water Resources Research*, 51, 1315–1332. <https://doi.org/10.1002/2014WR016569>
- Fahs, M., Ataie-Ashtiani, B., Younes, A., Simmons, C. T., & Ackerer, P. (2016). The Henry problem: New semianalytical solution for velocity-dependent dispersion. *Water Resources Research*, 52, 7382–7407. <https://doi.org/10.1002/2016WR019288>
- Fahs, M., Younes, A., & Mara, T. A. (2014). A new benchmark semi-analytical solution for density-driven flow in porous media. *Advances in Water Resources*, 70, 24–35. <https://doi.org/10.1016/j.advwatres.2014.04.013>
- Fajraoui, N., Fahs, M., Younes, A., & Sudret, B. (2017). Analyzing natural convection in porous enclosure with polynomial chaos expansions: Effect of thermal dispersion, anisotropic permeability and heterogeneity. *International Journal of Heat and Mass Transfer*, 115, 205–224. <https://doi.org/10.1016/j.ijheatmasstransfer.2017.07.003>
- Gingerich, S. B., Voss, C. I., & Johnson, A. G. (2017). Seawater-flooding events and impact on freshwater lenses of low-lying islands: Controlling factors, basic management and mitigation. *Journal of Hydrology*, 551, 676–688. <https://doi.org/10.1016/j.jhydrol.2017.03.001>
- Graf, T., & Boufadel, M. C. (2011). Effect of viscosity, capillarity and grid spacing on thermal variable-density flow. *Journal of Hydrology*, 400(1–2), 41–57. <https://doi.org/10.1016/j.jhydrol.2011.01.025>
- Guerrero-Martinez, F. J., Younger, P. L., Karimi, N., & Kyriakis, S. (2017). Three-dimensional numerical simulations of free convection in a layered porous enclosure. *International Journal of Heat and Mass Transfer*, 106, 1005–1013. <https://doi.org/10.1016/j.ijheatmasstransfer.2016.10.072>
- Henry (1964). Effects of dispersion on salt encroachment in coastal aquifer, seawater in coastal aquifers, (1613C), C70–C84.
- Hidalgo, J. J., & Carrera, J. (2009). Effect of dispersion on the onset of convection during CO₂ sequestration. *Journal of Fluid Mechanics*, 640, 441. <https://doi.org/10.1017/S0022112009991480>
- Hirasaki, G. J., & Hellums, J. D. (1968). A general formulation of the boundary conditions on the vector potential in three-dimensional hydrodynamics. *Quarterly of Applied Mathematics*, 26(3), 331–342. <https://doi.org/10.1090/qam/234676>
- Hirthe, E. M., & Graf, T. (2012). Non-iterative adaptive time-stepping scheme with temporal truncation error control for simulating variable-density flow. *Advances in Water Resources*, 49, 46–55. <https://doi.org/10.1016/j.advwatres.2012.07.021>
- Holzbecher, E. O. (1998). *Modeling density-driven flow in porous media*. Berlin: Springer. <https://doi.org/10.1007/978-3-642-58767-2>

- Hoteit, H., Ackerer, P., & Mosé, R. (2004). Nuclear waste disposal simulations: Couplex test cases. *Computational Geosciences*, 8(2), 99–124. <https://doi.org/10.1023/B:COMG.0000035074.37722.71>
- Hoteit, H., Ackerer, P., Mosé, R., Erhel, J., & Philippe, B. (2004). New two-dimensional slope limiters for discontinuous Galerkin methods on arbitrary meshes. *International Journal for Numerical Methods in Engineering*, 61(14), 2566–2593. <https://doi.org/10.1002/nme.1172>
- Hoteit, H., & Firoozabadi, A. (2018). Modeling of multicomponent diffusions and natural convection in unfractured and fractured media by discontinuous Galerkin and mixed methods. *International Journal for Numerical Methods in Engineering*, 114(5), 535–556. <https://doi.org/10.1002/nme.5753>
- Johannsen, K., Oswald, S., Held, R., & Kinzelbach, W. (2006). Numerical simulation of three-dimensional saltwater–freshwater fingering instabilities observed in a porous medium. *Advances in Water Resources*, 29(11), 1690–1704. <https://doi.org/10.1016/j.advwatres.2005.12.008>
- Kalejaiye, B. O., & Cardoso, S. S. S. (2005). Specification of the dispersion coefficient in the modeling of gravity-driven flow in porous media. *Water Resources Research*, 41, W10407. <https://doi.org/10.1029/2004WR003925>
- Kerrou, J., & Renard, P. (2010). A numerical analysis of dimensionality and heterogeneity effects on advective dispersive seawater intrusion processes. *Hydrogeology Journal*, 18(1), 55–72. <https://doi.org/10.1007/s10040-009-0533-0>
- Ketabchi, H., Mahmoodzadeh, D., Ataie-Ashtiani, B., Werner, A. D., & Simmons, C. T. (2014). Sea-level rise impact on fresh groundwater lenses in two-layer small islands. *Hydrological Processes*, 28(24), 5938–5953. <https://doi.org/10.1002/hyp.10059>
- Knorr, B., Xie, Y., Stumpp, C., Maloszewski, P., & Simmons, C. T. (2016). Representativeness of 2D models to simulate 3D unstable variable density flow in porous media. *Journal of Hydrology*, 542, 541–551. <https://doi.org/10.1016/j.jhydrol.2016.09.026>
- Kolditz, O., Görke, U.-J., Shao, H., Wang, W., & Bauer, S. (Eds.) (2016). *Thermo-hydro-mechanical-chemical processes in fractured porous media: Modelling and benchmarking*. Cham: Springer International Publishing. <https://doi.org/10.1007/978-3-319-29224-3>
- Koohbor, B., Fahs, M., Ataie-Ashtiani, B., Simmons, C. T., & Younes, A. (2018). Semianalytical solutions for contaminant transport under variable velocity field in a coastal aquifer. *Journal of Hydrology*, 560, 434–450. <https://doi.org/10.1016/j.jhydrol.2018.03.048>
- Langevin, C. D., Hughes, J. D., Banta, E., Provost, A., Niswonger, R., & Panday, S. (2017). MODFLOW 6, the U.S. Geological Survey Modular Hydrologic Model. U.S. Geological Survey. <https://doi.org/10.5066/F76Q1VQV>
- Langevin, C. D., Thorne, D. T., Dausman, A. M., Sukop, M. C., & Guo, W. (2008). *SEAWAT version 4: A computer program for simulation of multi-species solute and heat transport*. Reston, Virginia: U.S. Department of the Interior U.S. Geological Survey.
- Luz Neto, H., Quaresma, J. N. N., & Cotta, R. M. (2006). Integral transform solution for natural convection in three-dimensional porous cavities: Aspect ratio effects. *International Journal of Heat and Mass Transfer*, 49(23–24), 4687–4695. <https://doi.org/10.1016/j.ijheatmasstransfer.2006.04.028>
- Miller, C. T., Dawson, C. N., Farthing, M. W., Hou, T. Y., Huang, J., Kees, C. E., et al. (2013). Numerical simulation of water resources problems: Models, methods, and trends. *Advances in Water Resources*, 51, 405–437. <https://doi.org/10.1016/j.advwatres.2012.05.008>
- Moortgat, J., Amooie, M. A., & Soltanian, M. R. (2016). Implicit finite volume and discontinuous Galerkin methods for multicomponent flow in unstructured 3D fractured porous media. *Advances in Water Resources*, 96, 389–404. <https://doi.org/10.1016/j.advwatres.2016.08.007>
- Nassar, M. K., & Ginn, T. R. (2014). Impact of numerical artifact of the forward model in the inverse solution of density-dependent flow problem. *Water Resources Research*, 50, 6322–6338. <https://doi.org/10.1002/2013WR014672>
- Nguyen, V. T., Graf, T., & Guevara Morel, C. R. (2016). Free thermal convection in heterogeneous porous media. *Geothermics*, 64, 152–162. <https://doi.org/10.1016/j.geothermics.2016.05.006>
- Nield, D. A., Simmons, C. T., Kuznetsov, A. V., & Ward, J. D. (2008). On the evolution of salt lakes: Episodic convection beneath an evaporating saltlake. *Water Resources Research*, 44, W02439. <https://doi.org/10.1029/2007WR006161>
- Nield, D. A., & Bejan, A. (2017). *Convection in porous media*. Cham: Springer International Publishing. <https://doi.org/10.1007/978-3-319-49562-0>
- Niemi, A., Bear, J., & Bensabat, J. (Eds.) (2017). *Geological storage of CO₂ in deep saline formations* (Vol. 29). Dordrecht, Netherlands: Springer. <https://doi.org/10.1007/978-94-024-0996-3>
- Oswald, S., & Kinzelbach, W. (2004). Three-dimensional physical benchmark experiments to test variable-density flow models. *Journal of Hydrology*, 290(1–2), 22–42. <https://doi.org/10.1016/j.jhydrol.2003.11.037>
- Oswald, S., Kinzelbach, W., Greiner, A., & Brix, G. (1997). Observation of flow and transport processes in artificial porous media via magnetic resonance imaging in three dimensions. *Geoderma*, 80(3–4), 417–429. [https://doi.org/10.1016/S0016-7061\(97\)00064-5](https://doi.org/10.1016/S0016-7061(97)00064-5)
- Pau, G. S. H., Bell, J. B., Pruess, K., Almgren, A. S., Lijewski, M. J., & Zhang, K. (2010). High-resolution simulation and characterization of density-driven flow in CO₂ storage in saline aquifers. *Advances in Water Resources*, 33(4), 443–455. <https://doi.org/10.1016/j.advwatres.2010.01.009>
- Peyret, R. (2013). *Spectral methods for incompressible viscous flow*. New York: Springer Science & Business Media.
- Povich, T. J., Dawson, C. N., Farthing, M. W., & Kees, C. E. (2013). Finite element methods for variable density flow and solute transport. *Computational Geosciences*, 17(3), 529–549. <https://doi.org/10.1007/s10596-012-9330-2>
- Prasad, A., & Simmons, C. T. (2005). Using quantitative indicators to evaluate results from variable-density groundwater flow models. *Hydrogeology Journal*, 13(5–6), 905–914. <https://doi.org/10.1007/s10040-004-0338-0>
- Riley, M. F., & Firoozabadi, A. (1998). Compositional variation in hydrocarbon reservoirs with natural convection and diffusion. *AIChE Journal*, 44(2), 452–464. <https://doi.org/10.1002/aic.690440221>
- Sachse, A., Rink, K., He, W., & Kolditz, O. (2015). *OpenGeoSys-Tutorial*. Cham: Springer International Publishing. <https://doi.org/10.1007/978-3-319-13335-5>
- Schneider, A., Kröhn, K.-P., & Püschel, A. (2012). Developing a modelling tool for density-driven flow in complex hydrogeological structures. *Computing and Visualization in Science*, 15(4), 163–168. <https://doi.org/10.1007/s00791-013-0207-2>
- Shao, Q., Fahs, M., Younes, A., & Makradi, A. (2015). A high-accurate solution for Darcy-Brinkman double-diffusive convection in saturated porous media. *Numerical Heat Transfer, Part B: Fundamentals*, 69(1), 26–47. <https://doi.org/10.1080/10407790.2015.1081044>
- Shao, Q., Fahs, M., Younes, A., Makradi, A., & Mara, T. (2016). A new benchmark reference solution for double-diffusive convection in a heterogeneous porous medium. *Numerical Heat Transfer, Part B: Fundamentals*, 70(5), 373–392. <https://doi.org/10.1080/10407790.2016.1215718>
- Simmons, C. T., Bauer-Gottwein, P., Graf, T., Kinzelbach, W., Kooi, H., Li, L., et al. (2010). Variable density groundwater flow: From modelling to applications. In H. Wheeler, S. Mathias, & X. Li (Eds.), *Groundwater modelling in arid and semi-arid areas* (pp. 87–118). Cambridge: Cambridge University Press. <https://doi.org/10.1017/CBO9780511760280.008>
- Simmons, C. T. (2005). Variable density groundwater flow: From current challenges to future possibilities. *Hydrogeology Journal*, 13(1), 116–119. <https://doi.org/10.1007/s10040-004-0408-3>
- Sivasankaran, S., Kandaswamy, P., & Ng, C. O. (2008). Double diffusive convection of anomalous density fluids in a porous cavity. *Transport in Porous Media*, 71(2), 133. <https://doi.org/10.1007/s11242-007-9114-7-145>

- Stoeckl, L., Walther, M., & Graf, T. (2016). A new numerical benchmark of a freshwater lens. *Water Resources Research*, 52, 2474–2489. <https://doi.org/10.1002/2015WR017989>
- Therrien, R., McLaren, R. G., Sudick, E. A., & Panda, S. M. (2010). HydroGeoSphere: A Three-dimensional numerical model describing fully-integrated subsurface and surface flow and solute transport. Waterloo, Ont., Canada: University of Waterloo. Retrieved from <https://www.ggl.ulaval.ca/fileadmin/ggl/documents/rtherrien/hydrogeosphere.pdf>
- van Reeuwijk, M., Mathias, S. A., Simmons, C. T., & Ward, J. D. (2009). Insights from a pseudospectral approach to the Elder problem. *Water Resources Research*, 45, W04416. <https://doi.org/10.1029/2008WR007421>
- Voss, C. I., & Provost, A. M. (2010). *A model for saturated-unsaturated, variable-density ground-water flow with solute or energy transport*. Reston, Virginia: U.S. Department of the Interior U.S. Geological Survey. Retrieved from <http://water.usgs.gov/nrp/gwsoftware>
- Voss, C. I., Simmons, C. T., & Robinson, N. I. (2010). Three-dimensional benchmark for variable-density flow and transport simulation: Matching semi-analytic stability modes for steady unstable convection in an inclined porous box. *Hydrogeology Journal*, 18(1), 5–23. <https://doi.org/10.1007/s10040-009-0556-6>
- Wang, L., Nakanishi, Y., Hyodo, A., & Suekane, T. (2016). Three-dimensional structure of natural convection in a porous medium: Effect of dispersion on finger structure. *International Journal of Greenhouse Gas Control*, 53, 274–283. <https://doi.org/10.1016/j.ijggc.2016.08.018>
- Wang, Q. W., Yang, J., Zeng, M., & Wang, G. (2010). Three-dimensional numerical study of natural convection in an inclined porous cavity with time sinusoidal oscillating boundary conditions. *International Journal of Heat and Fluid Flow*, 31(1), 70–82. <https://doi.org/10.1016/j.ijheatfluidflow.2009.11.005>
- Werner, A. D., Bakker, M., Post, V. E. A., Vandenbohede, A., Lu, C., Ataie-Ashtiani, B., et al. (2013). Seawater intrusion processes, investigation and management: Recent advances and future challenges. *Advances in Water Resources*, 51, 3–26. <https://doi.org/10.1016/j.advwatres.2012.03.004>
- Xie, Y., Simmons, C. T., & Werner, A. D. (2011). Speed of free convective fingering in porous media. *Water Resources Research*, 47, W1150. <https://doi.org/10.1029/2011WR010555>
- Xie, Y., Simmons, C. T., Werner, A. D., & Diersch, H.-J. G. (2012). Prediction and uncertainty of free convection phenomena in porous media. *Water Resources Research*, 48, W02535. <https://doi.org/10.1029/2011WR011346>
- Younes, A., Ackerer, P., & Delay, F. (2010). Mixed finite elements for solving 2-D diffusion-type equations. *Reviews of Geophysics*, 48, RG1004. <https://doi.org/10.1029/2008RG000277>
- Younes, A., Fahs, M., & Ahmed, S. (2009). Solving density driven flow problems with efficient spatial discretizations and higher-order time integration methods. *Advances in Water Resources*, 32(3), 340–352. <https://doi.org/10.1016/j.advwatres.2008.11.003>
- Zhang, H., & Schwartz, F. W. (1995). Multispecies contaminant plumes in variable density flow systems. *Water Resources Research*, 31(4), 837–847. <https://doi.org/10.1029/94WR02567>
- Zhu, Q. Y., Zhuang, Y. J., & Yu, H. Z. (2017). Entropy generation due to three-dimensional double-diffusive convection of power-law fluids in heterogeneous porous media. *International Journal of Heat and Mass Transfer*, 106, 61–82. <https://doi.org/10.1016/j.ijheatmasstransfer.2016.10.050>